Compressive Loading and Modeling of Stitched Composite Stiffeners

Frank A. Leone, Jr.[1], Dawn C. Jegley[2]
NASA Langley Research Center, Hampton, VA, 23601, USA

Kim A. Linton[3]
The Boeing Company, Seal Beach, CA, 90740, USA

A series of single-frame and single-stringer compression tests were conducted at NASA Langley Research Center on specimens harvested from a large panel built using the Pultruded Rod Stitched Efficient Unitized Structure (PRSEUS) concept. Different frame and stringer designs were used in fabrication of the PRSEUS panel. In this paper, the details of the experimental testing of single-frame and single-stringer compression specimens are presented, as well as discussions on the performance of the various structural configurations included in the panel. Nonlinear finite element models were developed to further understand the failure processes observed during the experimental campaign.

I. Introduction

As part of the NASA Environmentally Responsible Aviation (ERA) Project, researchers at NASA Langley Research Center (LaRC) and The Boeing Company (Boeing) worked together to develop technology to support lighter, more fuel-efficient commercial transport aircraft. A major milestone for the ERA Project was to design, build and test a 30-foot-long multi-bay box (MBB) test article that was representative of an 80%-scale center section of a hybrid wing body (HWB) vehicle. A sketch of the MBB with the forward upper and lower bulkhead panels removed is shown in Fig. 1. A detailed description of the steps in the multi-year process to develop this new lightweight composites concept is presented in Ref. 1.

The MBB test article contained 11 large, out-of-autoclave cured, carbon/epoxy panels built using the Pultruded Rod Stitched Efficient Unitized Structure (PRSEUS) concept.[2] PRSEUS is an enabling technology for HWB architectures, due to the ability of the concept to support a pressurized, non-circular fuselage efficiently for both cost and weight. The primary motivation for MBB development and testing was to demonstrate both the manufacturability for large-scale components and the performance and strength of the structure.[3] This new approach exploits the advantages of stitched composites by integrating the skin, frames, stringers, tear straps, and T-caps together into a single dry, self-supporting preform assembly. The integrated preform is then infused and co-cured in a single oven cure step using a vacuum-assisted resin transfer molding process with high-precision Invar outer mold line (OML) tooling. An exploded view of the intersection of a PRSEUS frame and stringer is shown in Fig. 2. Further details of the fabrication methodology for stitched composites are presented in Ref. 4.

The 11 stitched panels of the MBB test article were fabricated by Boeing at their facility in Huntington Beach, CA, and subsequently assembled into the MBB at the Boeing C-17 final assembly facility in Long Beach, CA. The MBB was tested in the Combined Loads Test System (COLTS) facility at LaRC in April through June 2015. The MBB was subjected to combinations of internal pressure loading and mechanical loading that were representative of the design limit loads and design ultimate loads of an HWB aircraft for various critical flight conditions. Testing of the MBB is documented in Ref. 5.

During fabrication of the panels for the MBB, ideas were developed about how to improve the design and further develop stitched structures for future applications. Therefore, an additional panel was fabricated to test some of these new designs. A second center keel panel, based on the MBB center keel panel, was fabricated by Boeing and delivered to LaRC in February 2015. The primary motivation for fabricating this alternate center keel panel was to evaluate

[1] Aerospace Engineer, Structural Mechanics and Concepts Branch, MS 190, Member.
[2] Senior Aerospace Engineer, Structural Mechanics and Concepts Branch, MS 190, Associate Fellow.
[3] Senior Design Engineer, Advanced Structures, Boeing Research & Technology.

the structural performance of different configurations of the frames, stringers, and T-caps, as well as to develop the necessary fabrication processes and procedures for these new configurations.

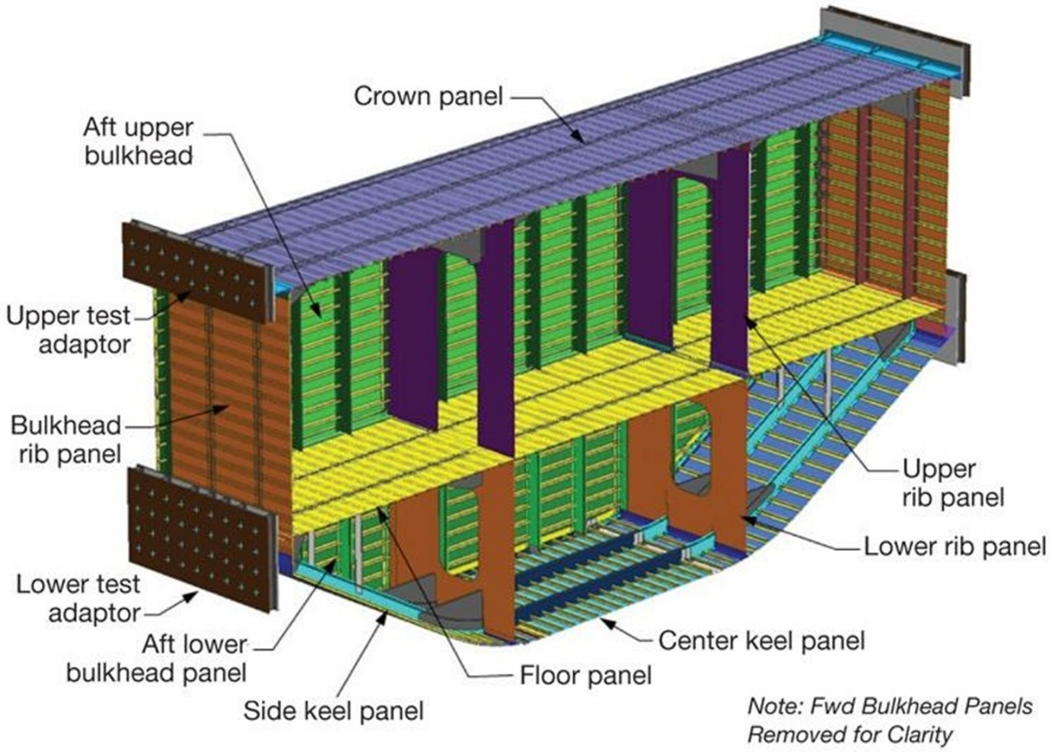

Figure 1. MBB test article components.

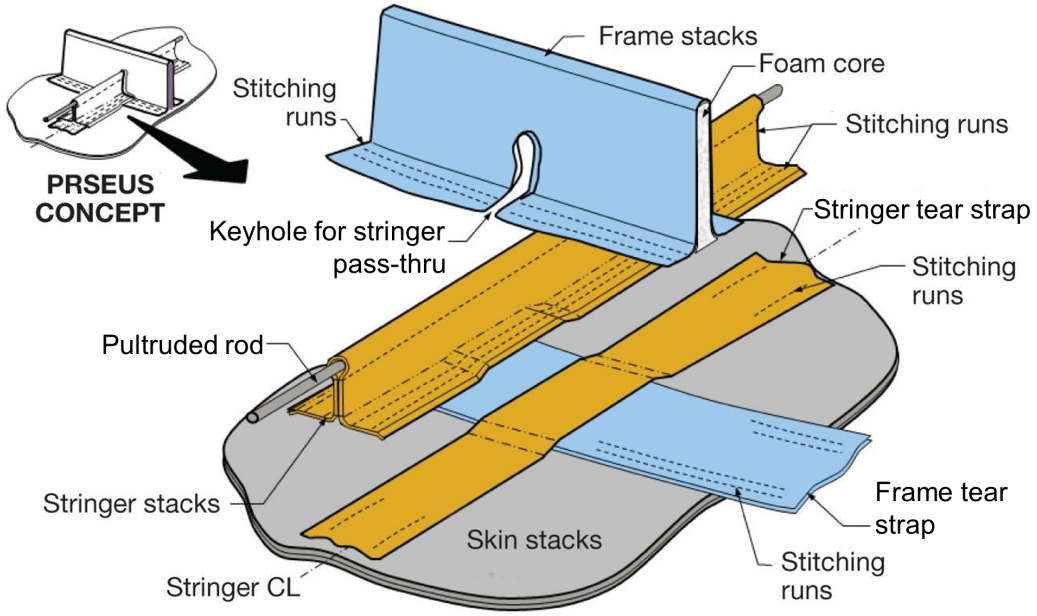

Figure 2. PRSEUS concept components.

This paper focuses on a set of single-frame and single-stringer compression specimens that were harvested from the alternate center keel panel. This paper presents details regarding the test specimens, the experimental procedure used to evaluate the specimens, and a discussion of the experimental results. Separate reports are available that focus on additional specimens harvested from the alternate center keel panel, including T-cap tension and bending specimens[6] and stringer rod push-out specimens.[7]

II. Alternate Center Keel Panel

The inner mold line (IML) surface of the alternate MBB center keel panel is shown in Fig. 3. The panel measured 71.9-inches long and 75.4-inches wide. The panel was made from a combination of dry carbon warp-knit fabric, pultruded rods, foam core, and stitching threads.

The skin and most parts of the stiffeners were made from carbon fiber layers with a (44/44/12) fiber architecture, where the values are percentages of (0/$\pm$45/90) degree plies. This material grouping, known as Class 72, Type 1 pre-kitted stacks, was the same material used in the MBB.[2] Each of these stacks has a nominal cured thickness of 0.052 inches. Standard modulus Toho HTA40E13 carbon fibers were used in the Class 72 stacks. A second material grouping, known as Class 101, Type 3, was included in the alternate center keel panel. The Class 101 pre-kitted stacks have a stacking sequence of [+30/0/$-$30/0] and nominal cured thickness of 0.021 inch. IMS65 E23, Toho Tenax-E 24K intermediate modulus fibers were used in the Class 101 stacks. Multiple stacks of the warp-knit materials were used to build up the desired part stiffness, strength, and configuration.

Through-the-thickness stitching was used to attach the stiffeners to the skin and, in selected locations, in the stiffener webs to form a dry, self-supporting preform. The preform was then infused with VRM-34 epoxy resin and cured in an oven. The panel contained three frames, 11 stringers, and two T-caps. Additional details regarding the design and fabrication of the alternate MBB center keel panel can be found in Ref. 8.

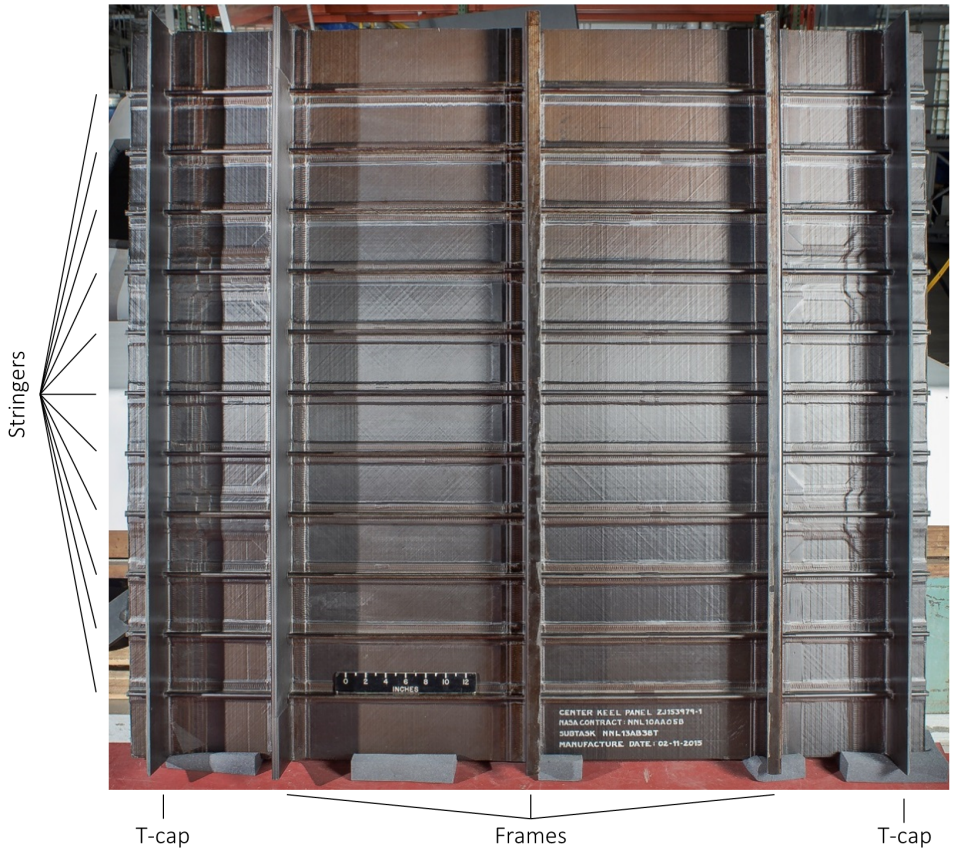

Figure 3. Photograph of the IML surface of the MBB alternate center keel panel, showing the stringers, frames, and T-caps.

A. Frame and Stringer Configurations

Three frame configurations and five stringer configurations were included in the alternate center keel panel, as shown in Fig. 4. All three frames were composed of the Class 72, Type 1 pre-kitted stacks. The frame configurations evaluated in this study are:

- A foam-filled frame (labeled F1 in Fig. 4), identical to the MBB test article frames, which served as the baseline configuration. Two stacks of material were wrapped around a 0.5-inch thick Rohacell 110 WF foam core to form the F1 frame;
- A tapered-blade frame (labeled F2 in Fig. 4), with minimum gauge regions (i.e., one stack thickness) in the web and built-up regions around the keyhole at the frame/stringer intersections. Additional damage-arresting stitching was included in the frame web. This configuration was designed to be comparable to frames in conventional barrel fuselage; and
- A constant-thickness blade frame (labeled F3 in Fig. 4), with a uniform four-stack thickness, designed to be an alternative to the foam-filled frame for an HWB fuselage with damage-arresting stitching in the web.

Cross-sectional schematics of the three frame configurations are shown in Fig. 5. All of the frame and frame tear strap stacks were aligned in the 0° direction, with the 0° direction being aligned along the length of the frames. The F1 tear straps were 4.25-inches wide and the F2 and F3 tear straps were 3.75-inches wide. The skin of the alternate center keel panel was composed of a stack of Class 72 material with the same orientation as the frame and frame tear strap stacks. The F1 frames measured approximately 6.125 inches in height from the OML surface to the top of the frame. The F2 and F3 frames measured approximately 4.75 inches in height from the OML surface to the top of the frame. The top flange in the F2 and F3 solid frames measured 1.50-inches wide.

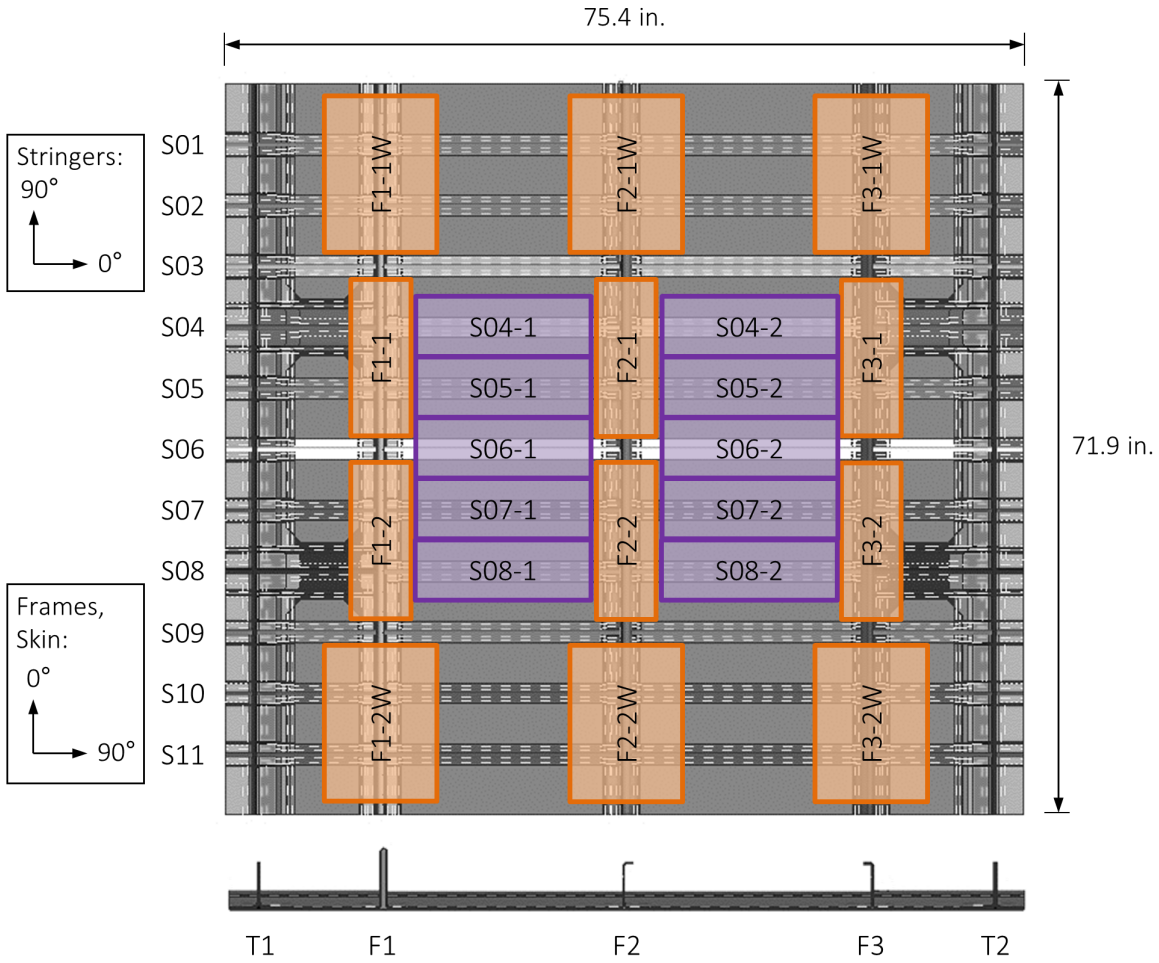

Figure 4. Single-frame compression and single-stringer compression specimen numbering and locations within the alternate center keel panel.

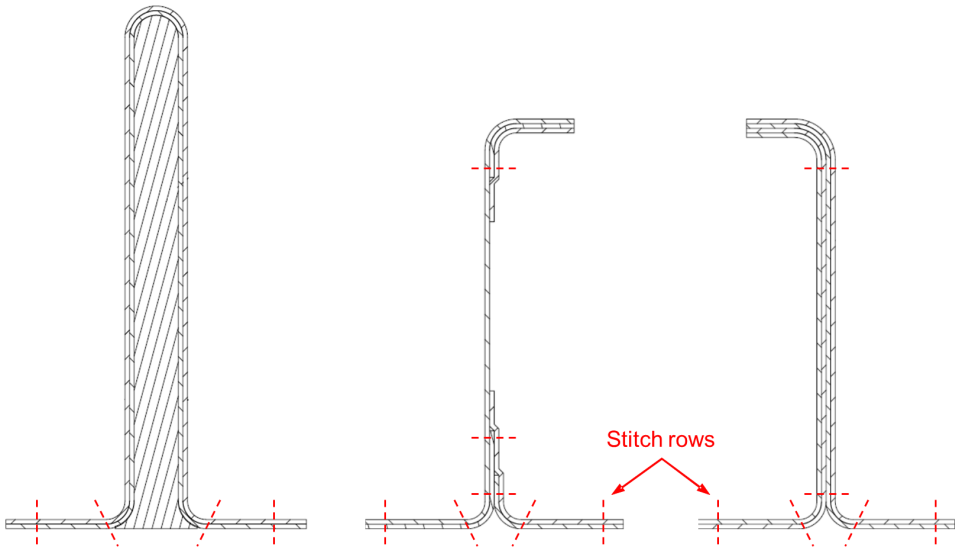

Figure 5. Cross-sectional views of the alternate keel panel frames. These cross-sections are representative of the frames between stringers. Additional doublers were used around the frame/stringer intersections in the tapered-blade frame.

The weight per unit length for the F1, F2, and F3 frame configurations are 0.113 lb/in, 0.068 lb/in, and 0.092 lb/in, respectively. These values include the frame, the foam for the F1 configuration, and the frame tear strap, but not the skin. Because the cross-sectional areas of the frames are not constant along their lengths, these weights were calculated using the average cross-sectional area for one stringer-to-stringer volume (i.e., 6.0 inches in length).

A PRSEUS stringer consists of a tear-shaped, unidirectional, carbon rod contained within a carbon/epoxy over-wrapping laminate. The overwrapping laminate also forms the web and bottom flange of the stringer. A schematic representation of a typical PRSEUS stringer cross-section which highlights each of these features is shown in Fig. 6. The five stringer configurations evaluated in this study varied in terms of stack material, stack orientation, and whether or not an adhesive layer was included between the rod and the overwrap. The five evaluated stringer configurations in Fig. 4 are:

- Class 72 overwrap (labeled S07, S10, S11);
- Class 72 overwrap with adhesive between the rod and overwrap (labeled S08, S09);
- Class 101 overwrap (labeled S01, S02, S05);
- Class 101 overwrap with adhesive between the rod and overwrap (labeled S03, S04); and
- Class 101 overwrap with a reversed stacking sequence (labeled S06).

The default configuration of the Class 101 stacks (i.e., S04 and S05) had the outer 0° fibers placed inward toward the rod. The reversed stacking sequence (i.e., S06) had the $+30^\circ$ fibers placed inward toward the rod. The adhesive used between the rod and the overwrap in stringers S03, S04, S08, and S09 was Cytec FM300 adhesive. The layer of adhesive was 0.015-inch thick.

The Class 72 stringers had two stacks in the web and one stack in the overwrap. The Class 101 stringers had four stacks in the web and two stacks in the overwrap. All of the stringer and stringer tear strap stacks were aligned in the 0° direction, with the 0° direction being aligned with the length of the stringers. Consequently, the material stacks in the stringers and the skin were oriented 90° apart. The pultruded rods in the stringers were 0.375 inch in diameter, and composed of Grafil 34-700WD standard modulus carbon fibers and PUL6 epoxy resin, with a teardrop shape. Each stringer measured approximately 1.875 inches in height from the OML surface to the top of the stringer overwrap.

B. Specimen Geometry

Twelve single-frame compression specimens were harvested from the alternate center keel panel. For each of the three frame configurations, two specimens were cut to a width of 5.7 inches and two specimens were cut to a width of 10.0 inches. The frame specimens are each 16.0 inches in length, and contain two stringers. Examples of the F1, F2,

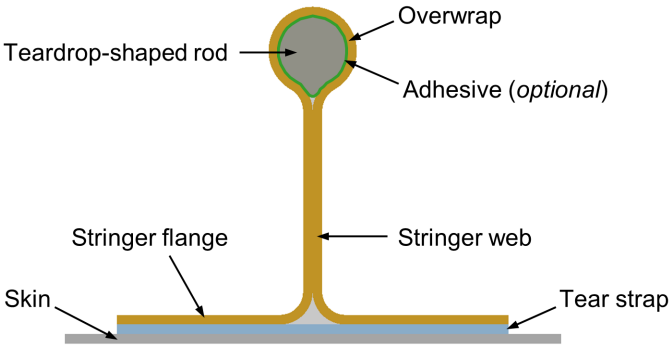

Figure 6. PRSEUS stringer cross-section.

and F3 single-frame compression specimens are shown in Figs. 7, 8, and 9, respectively.

Ten single-stringer compression specimens were harvested from the alternate center keel panel. The stringer specimens are each 5.90 inches in width and 17.5 inches in length. An example of a single-stringer compression specimen is shown in Fig. 10. The numbering of the single-frame compression and single-stringer compression specimens and the locations from which they were taken in the alternate center keel panel are shown in Fig. 4.

To prevent end brooming, one inch on each end of each compression specimen was potted in Hysol EA 9394 paste adhesive. A rectangular steel frame surrounded the potting material with at least 1 inch of potting material between the specimen and the frame at all points.

C. Experiment

The compression specimens were tested in a 120-kip load frame, shown in Fig. 11a. All tests were conducted at room temperature. The specimens were quasi-statically, monotonically loaded to failure under displacement control. A stroke rate of 0.008 inch/minute was used. The specimens were positioned so that the cross-section centroid of the stiffener/skin system was aligned with the center of the load platens, and that the IML faced the wall behind the load frame.

In order to avoid premature buckling of the skin of the specimens in a global buckling mode, anti-buckling guides were used during the compression tests. Custom anti-buckling guides with gaps for the stringers were used for the single-frame compression tests. The anti-buckling guides were centered along the lengths of the specimens, leaving approximately equal gaps between the anti-buckling guides and the potting at each end.

The displacement and rotation of the top platen were monitored with three linear variable displacement transducers (LVDTs) during the tests, shown in Fig. 11b. The LVDTs used in the tests each had 0.25 inch of travel. The positions of the LVDTs on the top load platen, which were kept constant throughout the test campaign, are shown schematically in Fig. 12. The three vertical displacements measured by the LVDTs were used to define the applied displacement at the center of the specimen, rather than using the stroke output from the load frame.

The load cell, LVDT, and stroke data were recorded at a rate of 10 Hz during the tests. Load readings were zeroed before the top load platen was in contact with the specimens.

Two three-dimensional digital image correlation (DIC) systems were used to monitor the full-field deformation of the specimens during testing. The first DIC system (DIC 1 in Fig. 13) was used to monitor the OML surface The second DIC system (DIC 2 in Fig. 13) was used to monitor one side of the stiffener. For the F2 and F3 single-frame specimens, the second DIC system monitored the flat side of the stiffener. During the tests, the out-of-plane displacement and loading direction strain were monitored to check for buckling and local material failure, respectively. Images were captured at a rate of one frame per two seconds. Prior to testing, the regions to be monitored by the DIC systems were spray painted with a flat, black-on-white speckle pattern, typical of DIC setups. The regions monitored by the two DIC systems were illuminated with white light-emitting diode (LED) lights during the tests.

A high-speed camera was used to monitor one side of the stiffener, positioned opposite the second DIC system The image capture rates varied from 60,000 to 100,000 frames per second, depending on the field of view required for each specimen type. Prior to testing, the region to be monitored by the high-speed camera was spray painted with a flat white paint to allow for easier detection of surface cracks. The region monitored by the high-speed camera was illuminated with red LED lights. In order to avoid light leakage between the high-speed camera setup and the second DIC setup, a cardboard partition was placed between them and attached the top of the stiffeners.

a) Cross-sectional view

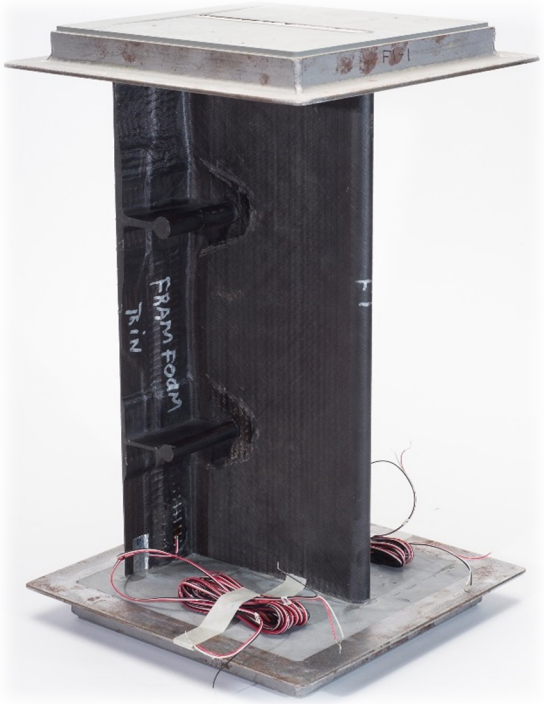

b) Side view

Figure 7. Foam-filled frame specimen (F1-1 is shown).

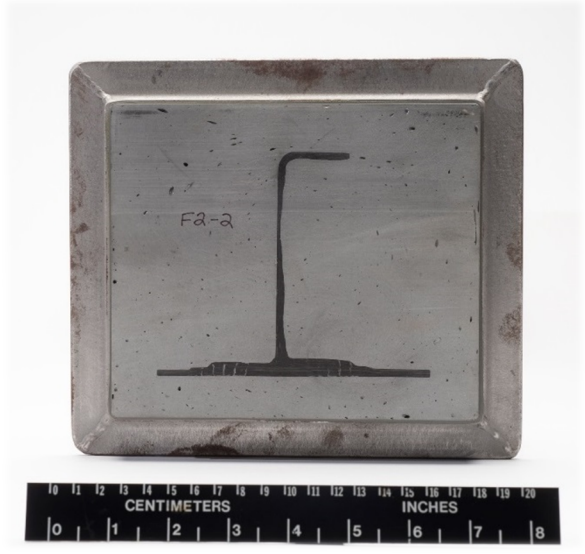

a) Cross-sectional view

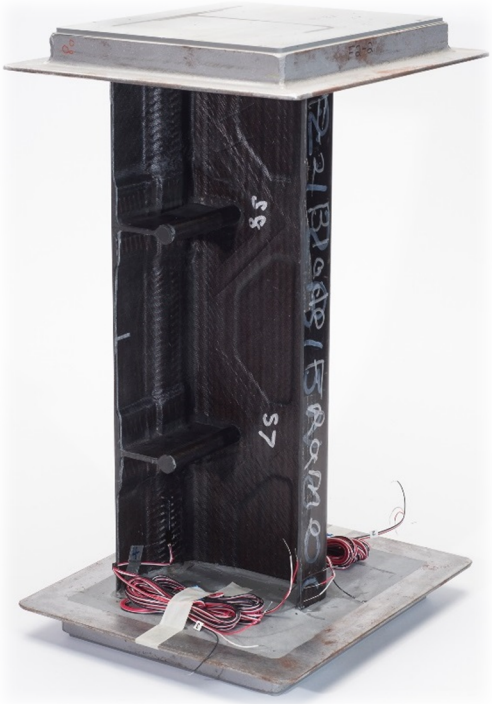

b) Side view

Figure 8. Tapered-blade frame specimen (F2-2 is shown).

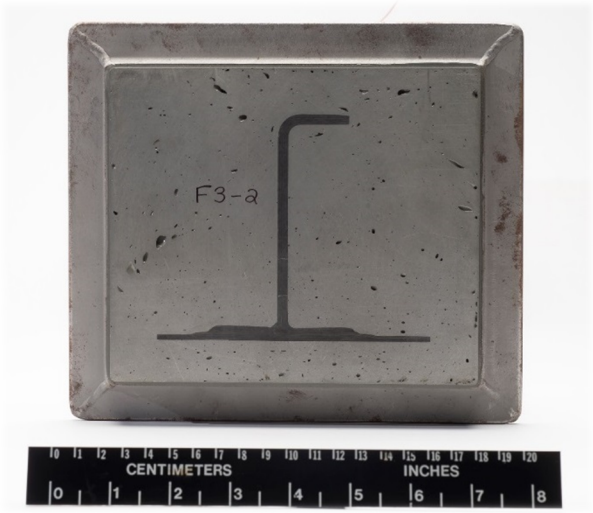

a) Cross-sectional view

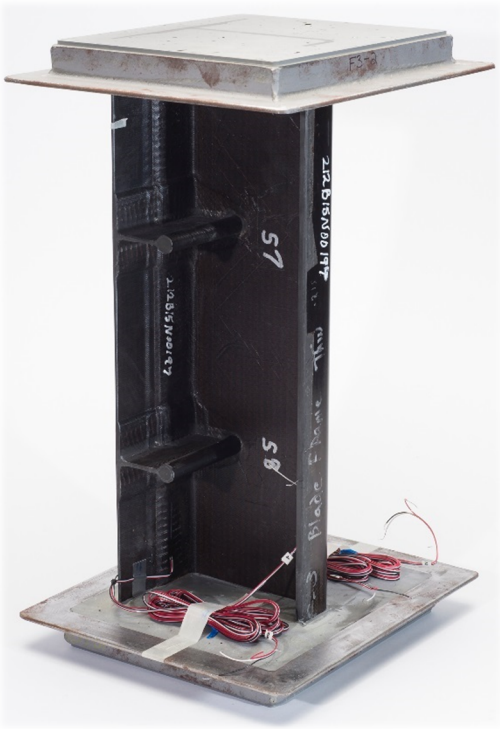

b) Side view

Figure 9. Constant-blade frame specimen (F3-2 is shown).

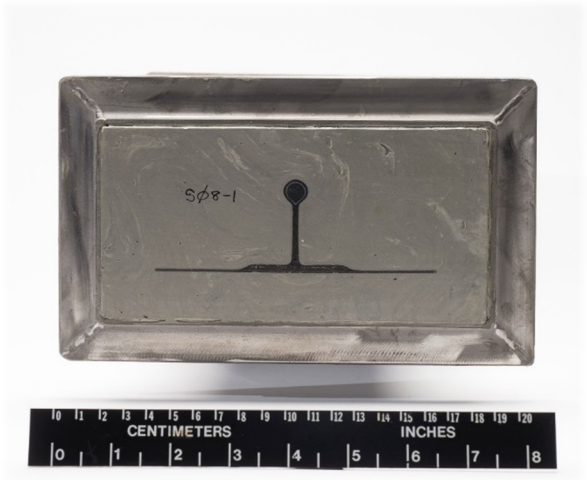

a) Cross-sectional view

b) Side view

Figure 10. Stringer specimen (S08-1 is shown).

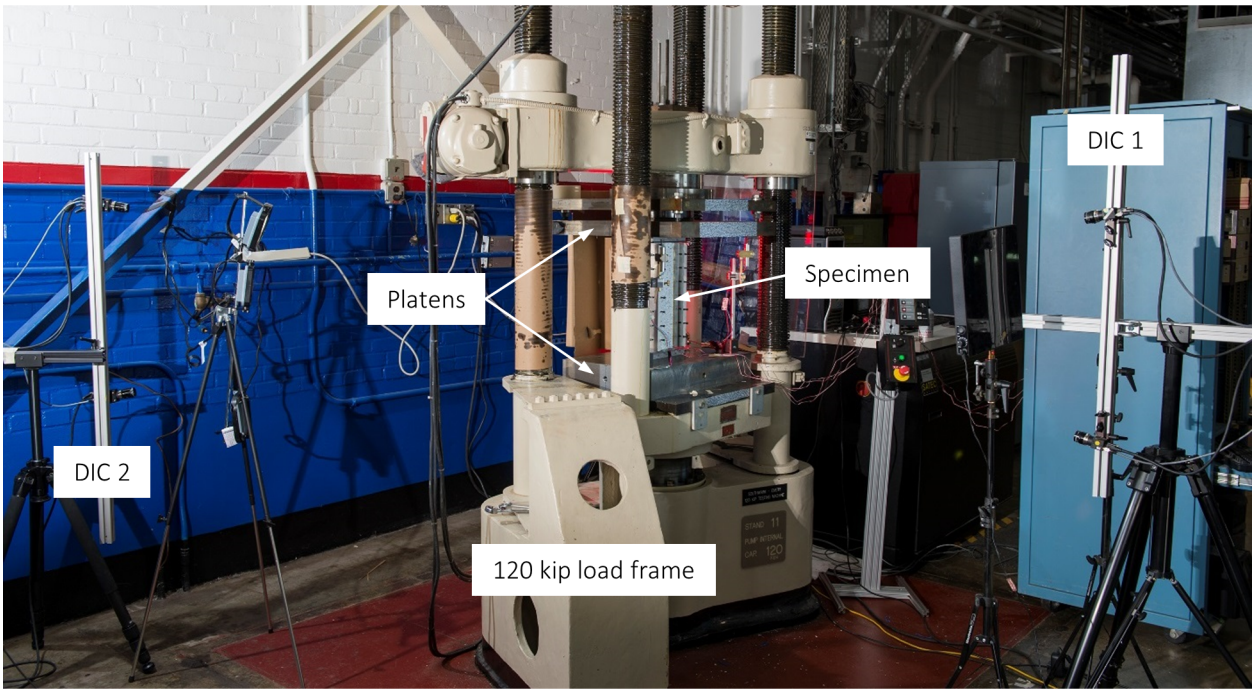

a) Load frame view

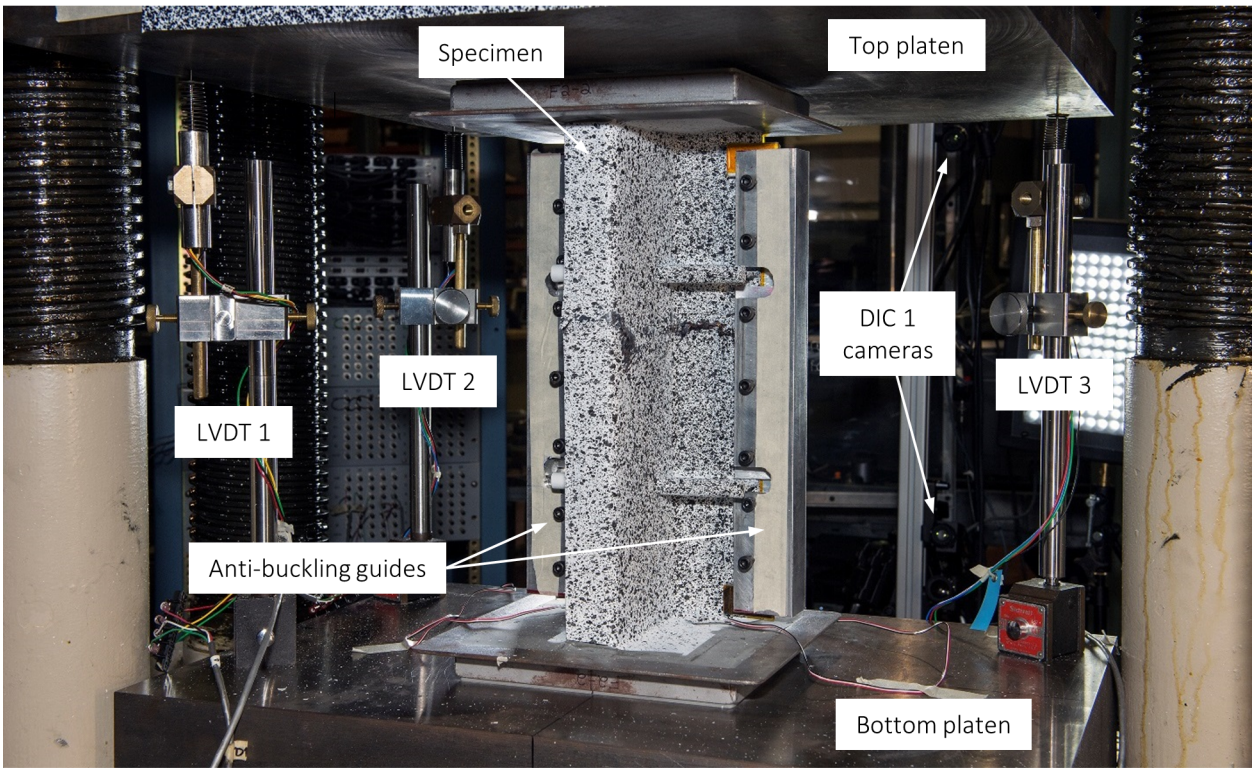

b) Specimen view

Figure 11. Experimental setup.

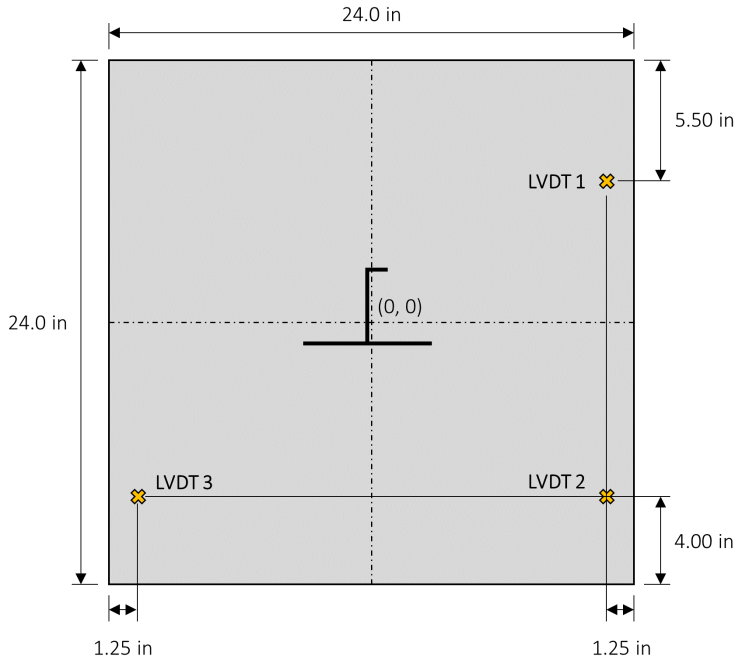

Figure 12. Positions of the three LVDTs on the top load platen.

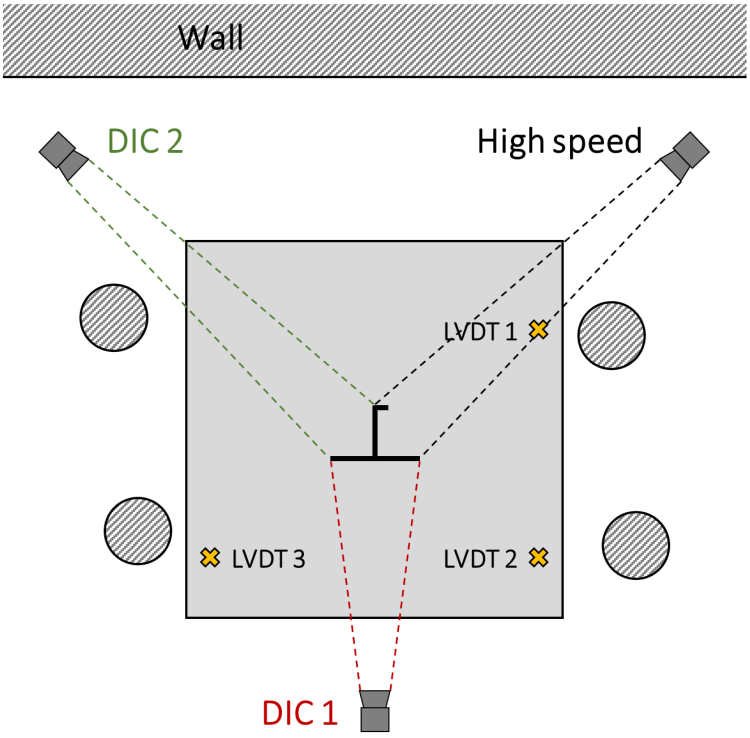

Figure 13. Measurement systems setup from the top-down view of the load frame.

III. Results and Discussion

A. Frame Specimen Tests

Eleven out of 12 single-frame compression specimens were successfully loaded to failure. Specimen F3-2 was not able to be properly balanced in the load frame, and was, therefore, not tested. Despite having only two replicates per specimen configuration, the results were consistent for each specimen configuration in both stiffness and strength. In addition, the differences between replicates for a given configuration were generally smaller than the differences between specimen configurations.

A summary of the failure loads and stiffnesses of the single-frame compression specimens is presented in Table 1. The F1 specimens had the greatest strength and stiffness in both the narrow and wide configurations. The constant-thickness blade frame specimens (F3) had comparable stiffnesses to the F1 specimens, but the strengths of the F3 specimens were 16% lower in the narrow configuration and 14% lower in the wide configuration. As expected, the lighter F2 specimens yielded lower compression failure load, strength, and stiffness results than the heavier configurations. As mentioned, the F2 frame configuration was designed for a tube and wing configuration, not an HWB, and was not intended to carry compressive loads as high as the other two configurations.

Table 1. Single-frame compression results.

Specimen	Failure load [kip]	Strength* [ksi]	Stiffness [kip/in]
F1-1	-117.8	-58.3	1179
F1-2	-107.3	-53.0	1179
F1-1W	-92.0	-41.0	1235
F1-2W	-97.4	-43.4	1237
F2-1	-57.5	-39.5	847
F2-2	-49.7	-34.2	843
F2-1W	-61.2	-36.5	931
F2-2W	-59.5	-35.5	927
F3-1	-86.6	-46.8	1099
F3-1W	-70.1	-33.8	1182
F3-2W	-79.8	-38.5	1194

* Calculated using the specimen average cross-sectional area, not including the foam in the F1 specimens.

The load-displacement histories for each of the tested single-frame specimens are shown in Fig. 14. The displacement in Fig. 14 is the displacement at the center of the top load platen, calculated using the positions and measured displacements of the three LVDTs. None of the specimens exhibited any major load drops prior to failing, with the exceptions of specimens F2-1 and F2-1W. All of the narrow frame specimens loaded linearly up to initial failure. Some load-displacement nonlinearity occurred in the wide F1 and F3 specimens beyond -60 kips, and beyond -30 kips in the wide F2 specimens.

Prior to failure, all of the frame specimens, narrow and wide, exhibited some degree of buckling within the minimum gauge skin sections along the edges of the specimens. Each of the wide frame specimens developed clear half-waves located between the stringers, and between the stringers and the potted ends of the specimens, as shown in Fig. 15a and 15b. The out-of-plane deformation of the narrow frame specimens was less consistent than the wide frame specimens in terms of the number of half-waves and their locations along the specimen edges. Examples of the out-of-plane displacements of the narrow frame specimens are shown in Fig. 15c and 15d. The magnitudes of the out-of-plane displacements in the skin of the narrow specimens were consistently less than those of the corresponding wide frame specimens.

No buckling of the F1 or F3 specimen frame webs occurred during the tests. The F2 specimens, however, were prone to buckling in the frame webs due to their reduced thicknesses. Each of the four F2 frame specimens exhibited buckling within the frame webs in the forms of five half-waves along the specimen length. Specimen F2-1 exhibited one load drop at -56.6 kips applied load, which corresponded to the rapid change in the magnitudes and shape of the two half-waves closest to the top of the specimen, as shown in Fig. 16. Specimen F2-1W exhibited two small load drops. The second load drop occurred at -56.2 kips applied load, and corresponded to a similar change in the

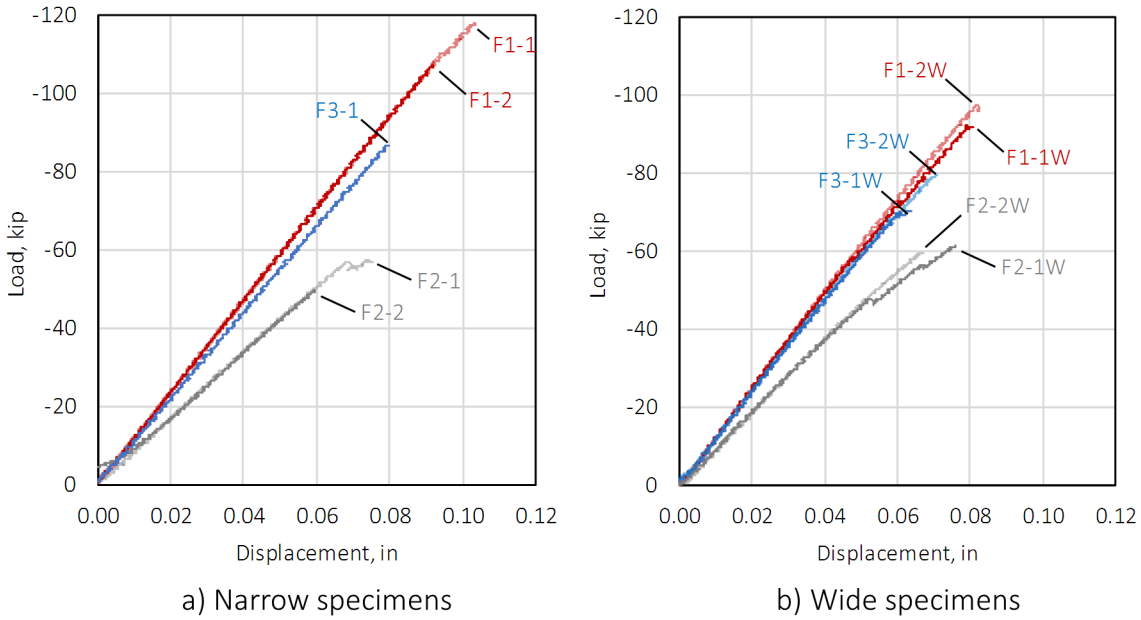

Figure 14. Frame compression specimen load-displacement responses.

magnitudes of the three central half-waves, as shown in Fig. 17. The locations of ultimate failure for specimens F2-1 and F2-1W later corresponded to the locations of these buckling-mode shape changes.

The exact location and path of the final specimen failures varied across specimen configurations and across replicates. However, in all cases, the final damage state within the skin extended the full width of the specimen along either the edge of a stringer flange or beneath one-half of a stringer flange (e.g., Fig. 18); no dominant failures occurred in the skin between the stringers.

For the F1 and F3 specimens, the failure path in the stiffener tended either to be coplanar with the skin failure (e.g., Fig. 19a), or to pass through the stringer keyhole (e.g., Fig. 19b). For all of the F1 and F3 failures which were captured via the high-speed camera system, the failures originated at the root of the frame near the frame/stringer intersections, and propagated up the frame web. The failure process of specimen F3-2W is representative of the F1 and F3 specimens, and is shown in Fig. 20. In the figure, select frames are shown in which significant changes in the damage state are visible. The time in microseconds (μs) between the first image and the subsequent images is shown in the subfigure captions.

For the F2 specimens, a combination of the built-up thickness around the stringer keyhole (visible in Fig. 8) and the through-the-thickness stitching prevented the failure path from passing through the keyhole. Instead, the observed failure paths connected the minimum gauge sections of the frame web and the stringer flange edges. The final F2 stiffener damage passed either between the two stringers (e.g., Fig. 19c) or between the potting and a stringer (e.g., Fig. 19d). The failure process of specimen F2-2W is representative of the F2 specimens, and is shown in Fig. 21. Damage was observed to initiate along the edge of the minimum-gauge region of the F2 frame web (Fig. 21b) and propagate along the stitch line along the stack termination in the frame web (Fig. 21c). The stitch line temporarily arrested the damage propagation (Fig. 21d) before ultimate failure (Fig. 21e).

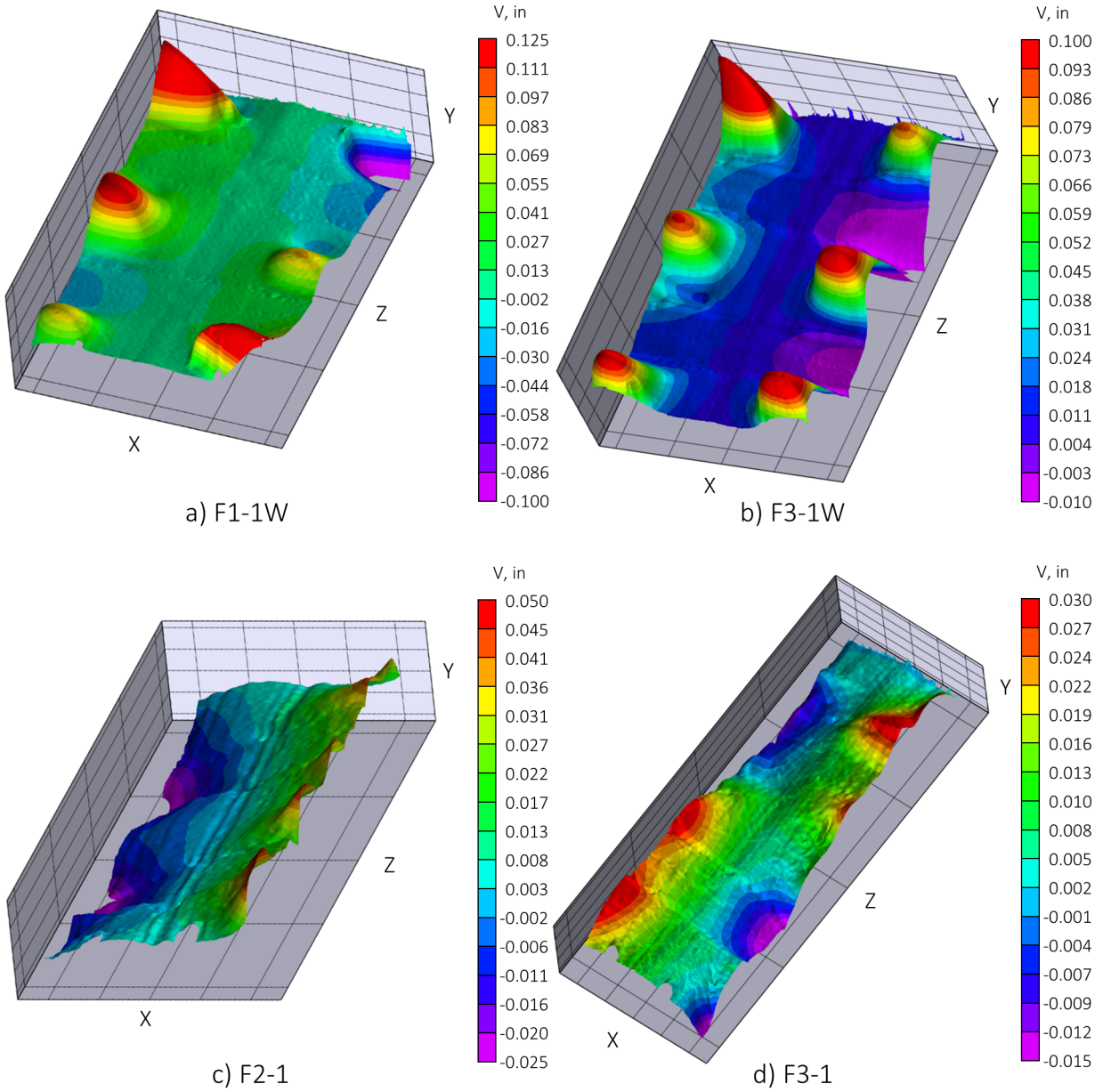

Figure 15. Out-of-plane deformation of the skins of selected single-frame compression specimens immediately before failure.

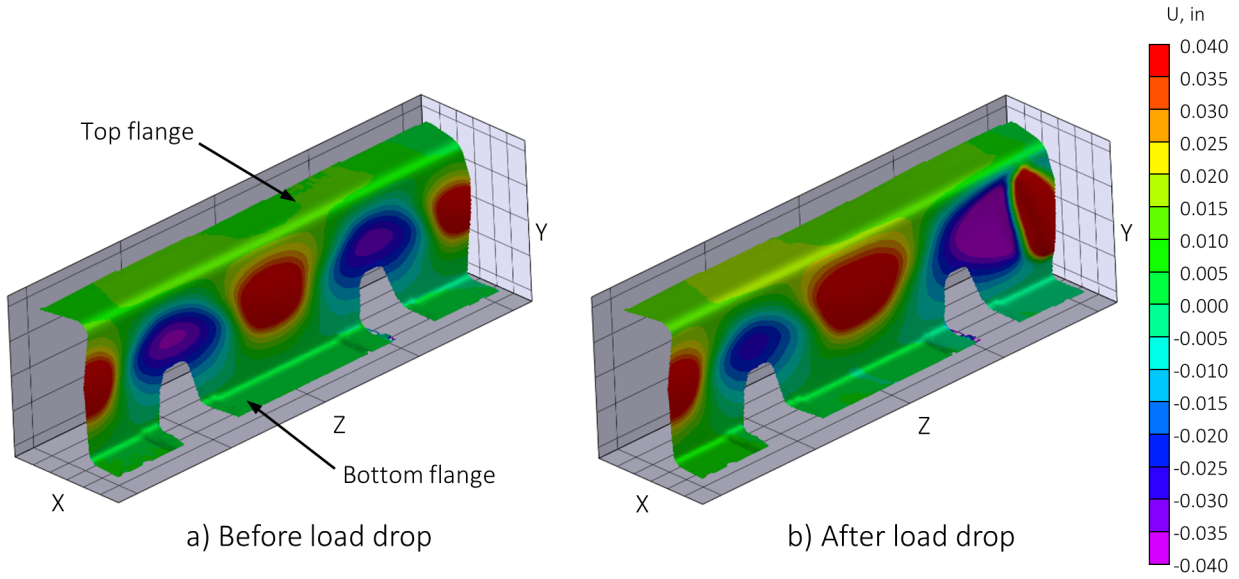

Figure 16. Out-of-plane deformation of the frame web in specimen F2-1.

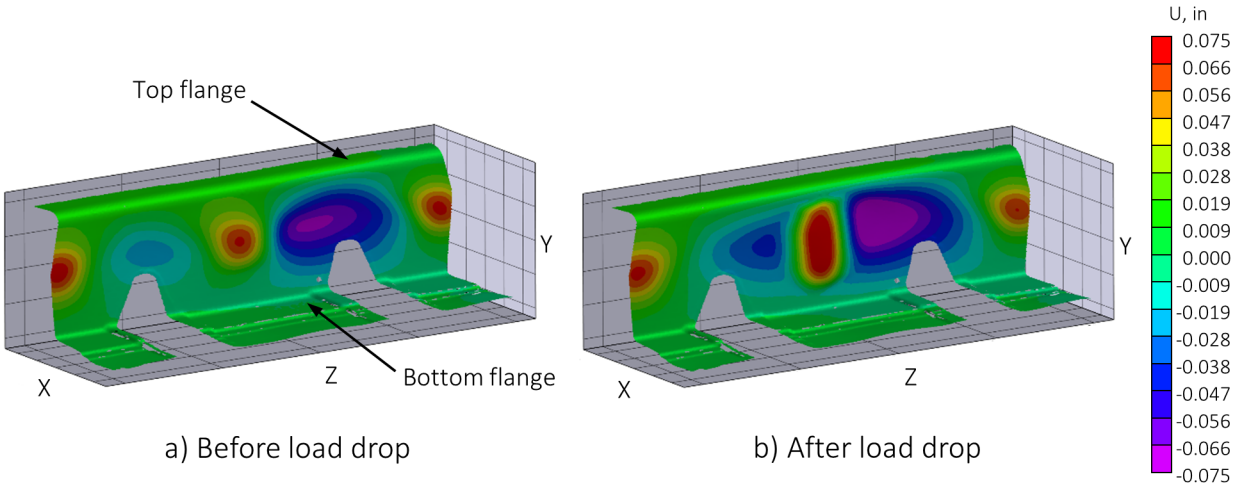

Figure 17. Out-of-plane deformation of the frame web in specimen F2-1W.

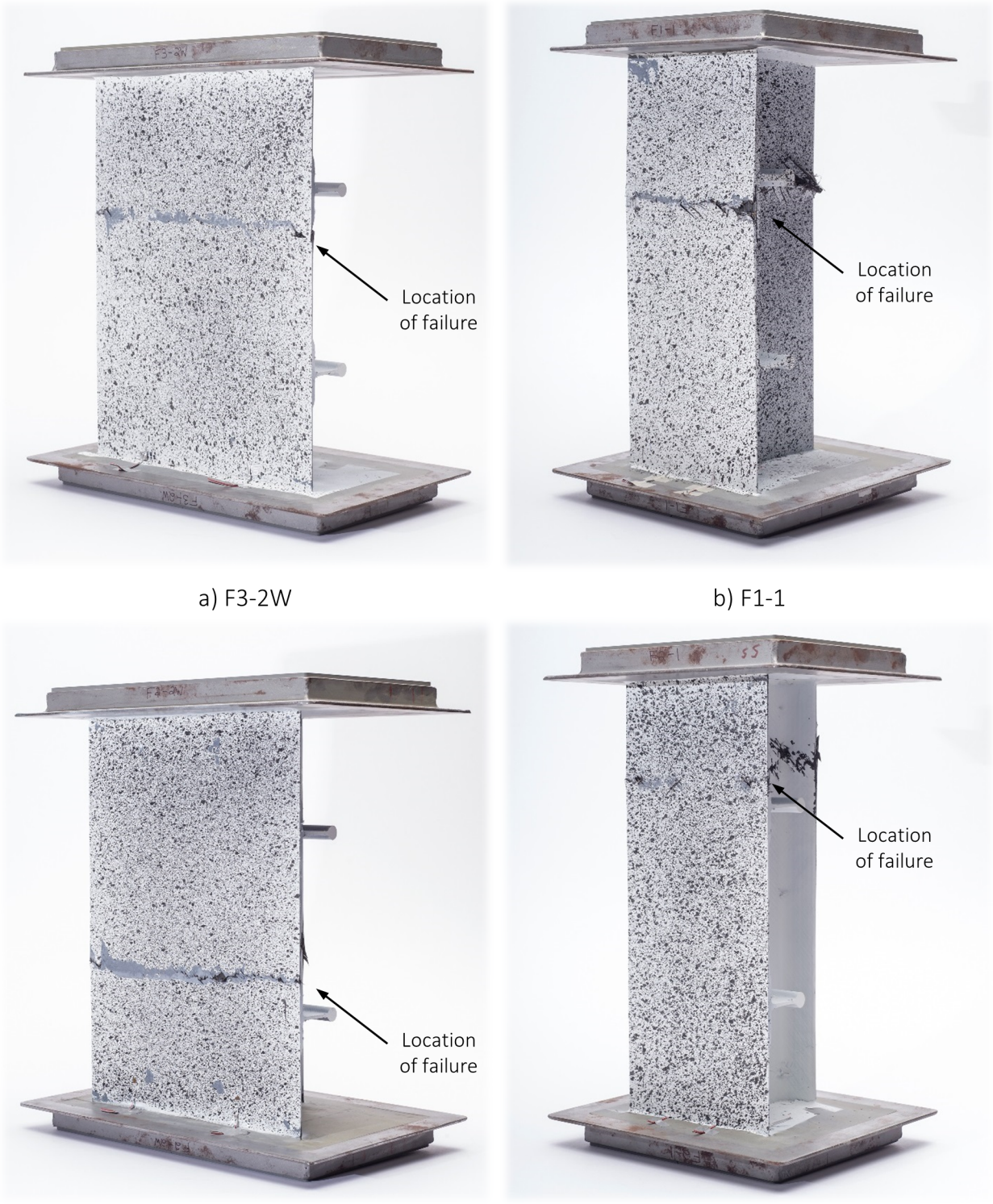

Figure 18. Locations of failure in the skins of a representative set of single-frame specimens, OML view.

Figure 19. Locations of failure in the stiffeners of a representative set of single-frame specimens, IML view.

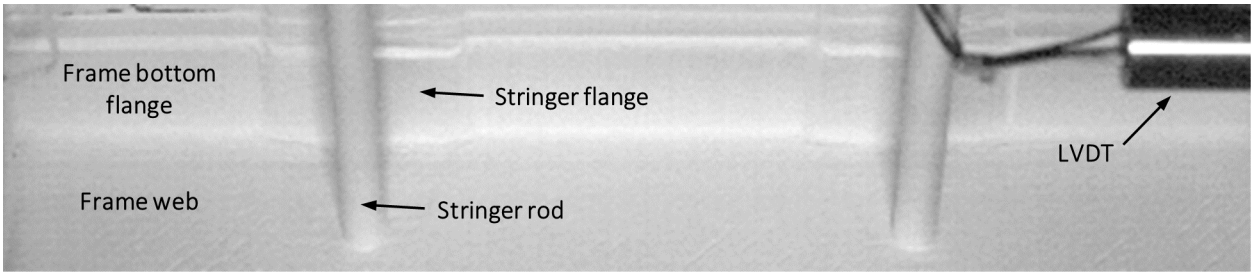

a) Δt = 0 μs

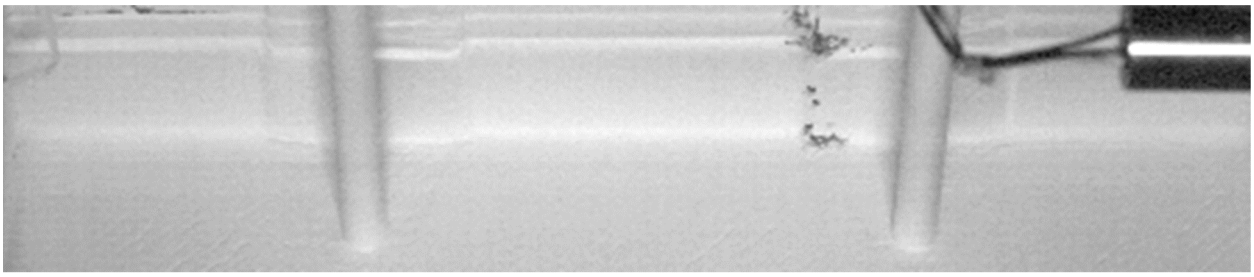

b) Δt = 166 μs

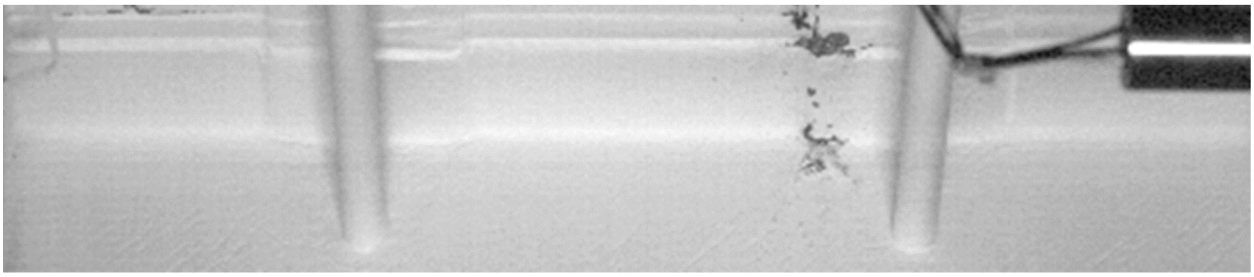

c) Δt = 1248 μs

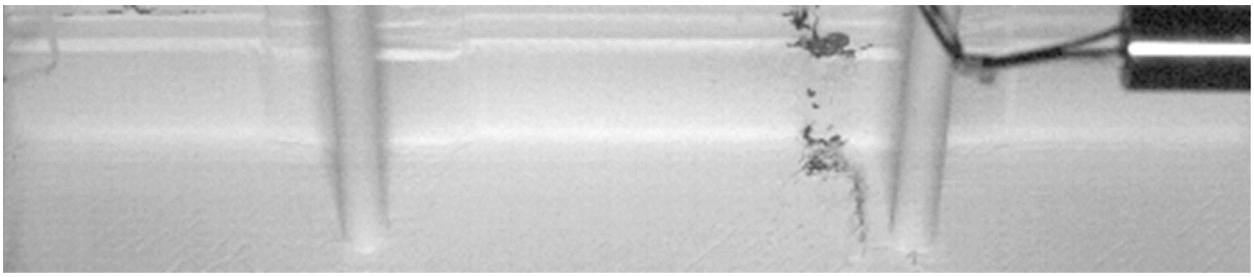

d) Δt = 1281 μs

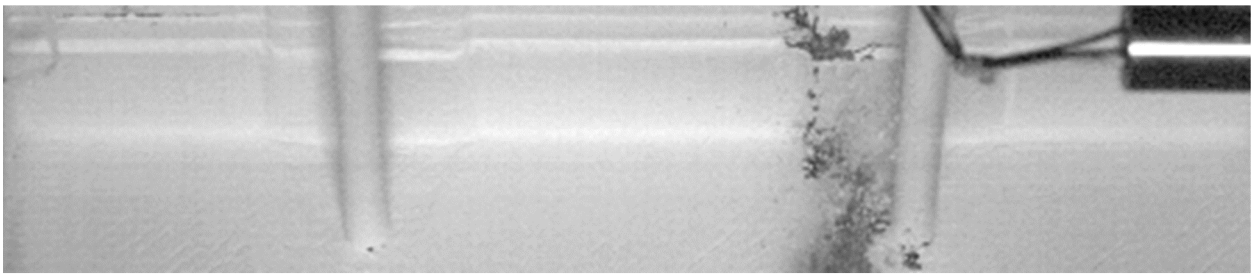

e) Δt = 1681 μs

Figure 20. High-speed photography images of the failure of specimen F3-2W.

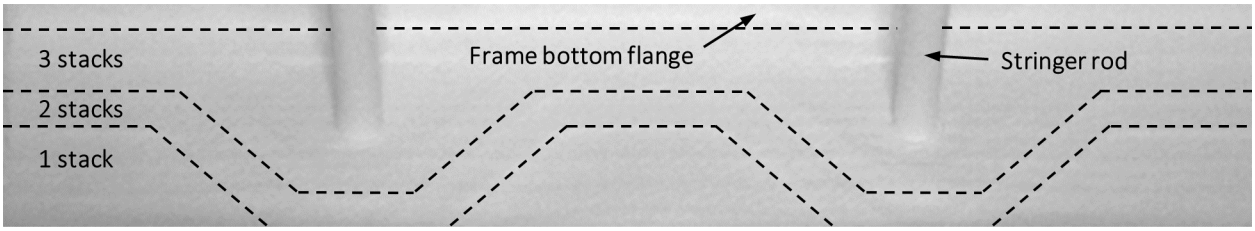

a) Δt = 0 μs

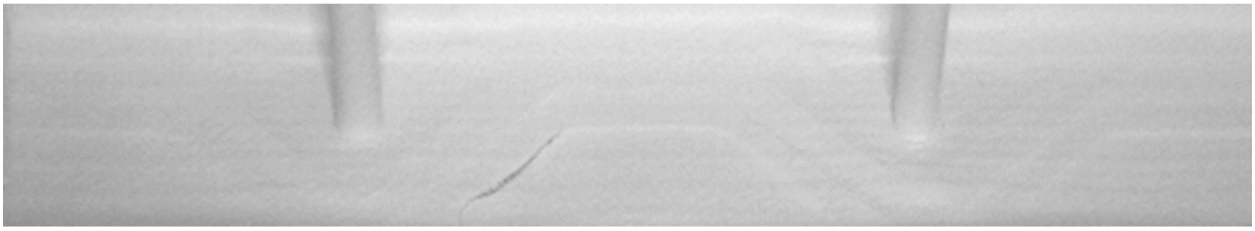

b) Δt = 100 μs

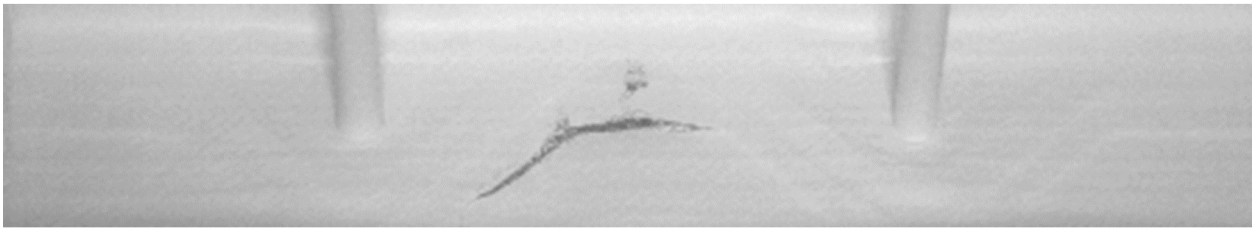

c) Δt = 329 μs

d) Δt = 629 μs

e) Δt = 3958 μs

Figure 21. High-speed photography images of the failure of specimen F2-2W.

B. Frame Specimen Models

Finite element models of the single-frame specimens were developed to further understand the failure processes observed in the single-frame tests. The analyses were performed using Abaqus/Standard 6.13-1[9] in a single static step. Because buckling was observed during the F2 specimen tests, the effects of geometric nonlinearity were included in each of the frame specimen analyses.

The stack materials in each model were represented by eight-node continuum shell elements (SC8R). The foam and rod materials were represented by eight-node solid elements (C3D8R). The through-the-thickness stitching was not included in these models. The models were each 14.5-inches long, meant to represent the material between the potted ends of the specimens, and 5.7-inches wide, meant to represent the narrow frame specimen configuration. Frictionless contact was assumed between the stringer web and overwrap and the keyholes in the frame web to allow for buckling of the frame web. The anti-buckling guides were modeled by constraining the y-direction displacement of the nodes on the OML skin surface in a 1-inch wide area from each free edge. The potted specimen ends were modeled by fully constraining the x-, y-, and z-direction displacements on one end, and the x- and y-direction displacements on the other. Compressive loads were introduced by monotonically displacing the nodes on one potted end of the model in the z-direction.

The predicted load-displacement responses of the F1, F2, and F3 narrow configuration analyses are shown in Fig. 22. In general, the analyses overpredicted the stiffness of the specimens. This overprediction of the stiffness can be attributed to the clamped boundary conditions at the potted ends of the specimen, and to the 14.5-inch length of the models and the 16.5-inch length of the specimens (including the potted ends). However, the relative stiffnesses of the different configurations was well captured by the analyses.

The compressive unnotched allowable of the Class 72 material stack is -79.2 ksi in the $0°$ direction and -37.9 ksi in the $90°$ direction.[2] Exceedance of -79.2 ksi in the $0°$ direction of the stack material was used as a conservative definition of failure for the frames. Using this definition of failure, initial and secondary failure locations were identified for each of the frame analyses. Stress contour plots for the stress component in the $0°$ stack direction that show the initial and secondary failure locations are shown in Fig. 23. For the F1, F2, and F3 frames, the initial failure was predicted to occur in the frame flange along the edges of the stringer flange at loads of -79 kips, -46 kips, and -68 kips, respectively. The location of the secondary failure prediction in the F1 and F3 analyses was at the top of the keyholes in the frame webs at -113 kips and -97 kips, respectively. Here, failure at the keyhole was assumed to occur when all elements through the thickness of the frame web exceeded the $0°$-direction unnotched allowable at a distance of 0.1 inch away from the hole edge. The location of the secondary failure prediction in the F2 analysis was at a corner between the 1-stack- and 2-stack-thick regions of the frame web, and was predicted to occur at -57 kips.

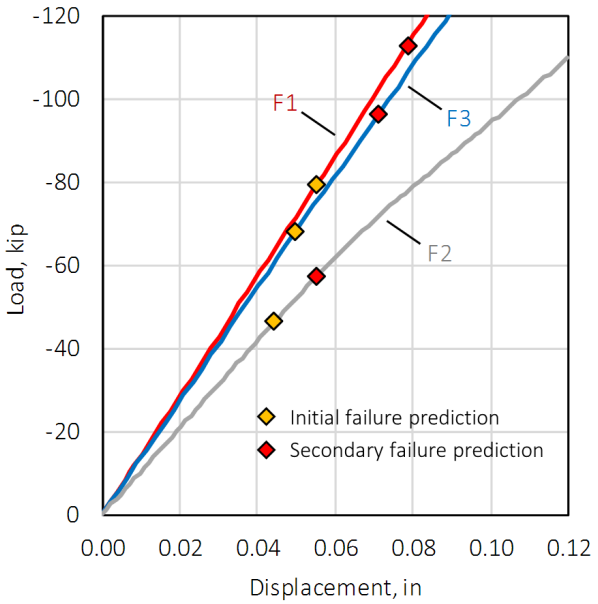

Figure 22. Load-displacement responses from the single-frame analyses for the narrow F1, F2, and F3 configurations.

For each of the frame analyses, the locations of the initial and secondary failure predictions are in agreement with the experimentally observed final failure paths shown in Fig. 19. In addition, the predicted loads for the primary and secondary failures bound the experimentally observed failure loads in Table 1.

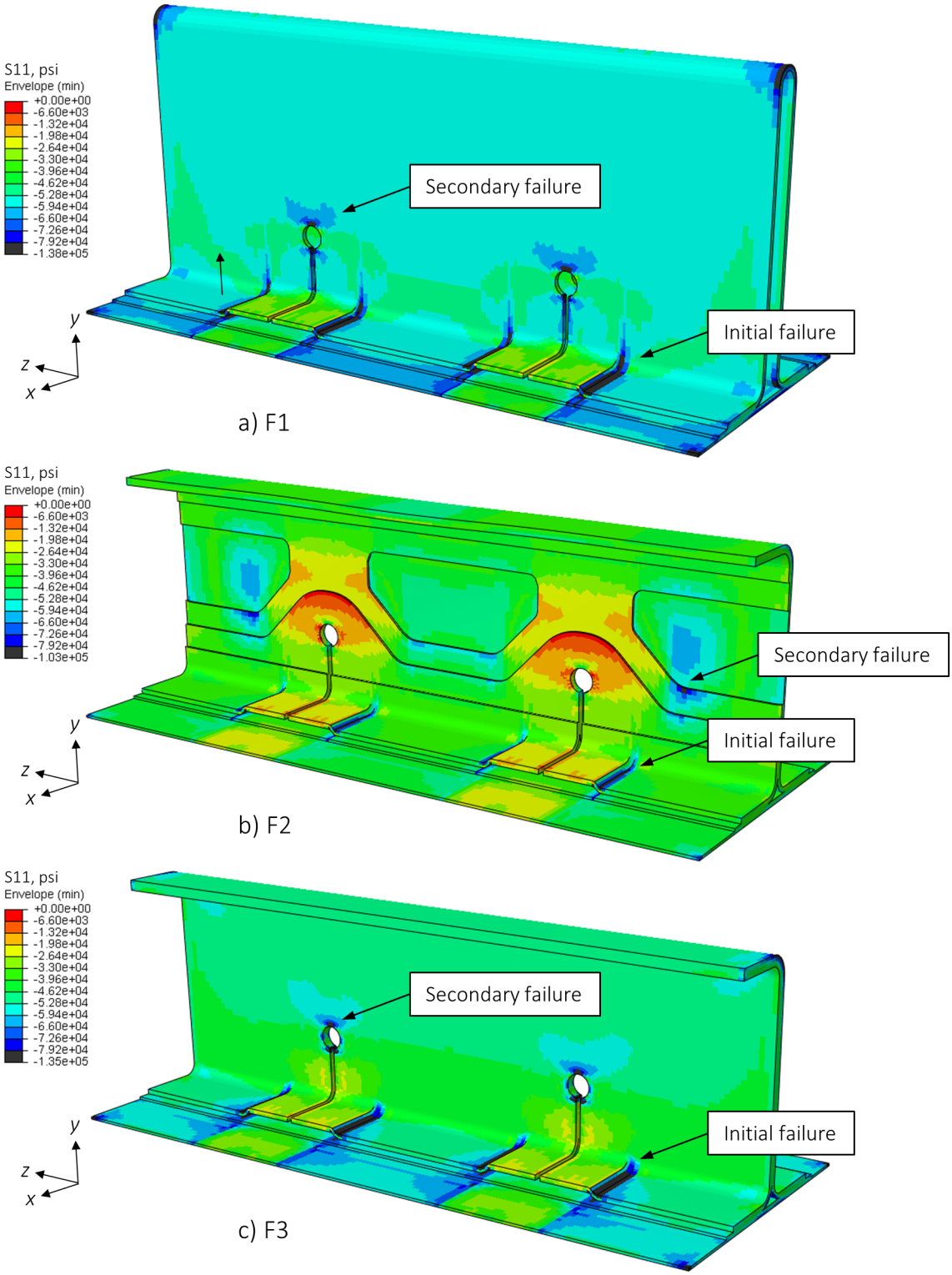

Figure 23. Stress contour plots from the single-frame analyses for the narrow F1, F2, and F3 configurations, shown at the exceedance of the unnotched allowable at the secondary failure location.

C. Stringer Specimen Tests

All 10 single-stringer compression specimens were successfully loaded to failure. In all cases, prior to failure, the stringer exhibited global buckling. In nine out of 10 cases, the buckling load was the test peak load. Additional deformation of the post-buckled single-stringer specimens was applied until failure. A summary of the buckling loads, failure loads, and stiffnesses of the single stringer compression specimens is presented in Table 2.

Table 2. Single-stringer compression results.

Specimen	Buckling load [kip]	Failure load* [kip]	Stiffness [kip/in]
S04-1	-28.9	-28.4	466
S04-2	-32.1	-29.8	466
S05-1	-28.4	-29.6	471
S05-2	-28.0	-27.2	471
S06-1	-26.7	-25.8	469
S06-2	-28.2	-25.3	466
S07-1	-31.9	-29.4	414
S07-2	-32.0	-28.4	411
S08-1	-34.5	-29.3	412
S08-2	-35.2	-30.6	417

* The highest load reached after buckling.

The load-displacement responses for each single-stringer compression specimen are plotted in Fig. 24, separated by stringer configuration. While too few replicates were tested to make strong statements regarding the relative performance of the different stringer configurations, some trends are apparent from the experimental results.

In general, the Class 101 stringers were stiffer than the Class 72 stringers. In addition, the presence of adhesive between the rod and the stringer overwrap did not have any appreciable effect on the stringer stiffness for either material system, as expected. In terms of buckling load, the Class 72 stringers performed better than their Class 101 counterparts, with an average buckling load of -33.4 kips compared to -28.7 kips. The presence of the adhesive did not have an appreciable effect on the strength of the Class 101 specimens, but the Class 72 specimens with adhesive had buckling loads 9% higher than the Class 72 specimens without adhesive. The reversal of the stacking sequence of the Class 101 overwrap in stringer S06 did not significantly affect either the stiffness or buckling load of the specimens. However, the postbuckled failure loads of the S06 specimens were 11% lower than the other Class 101 specimens.

As mentioned, each of the single-stringer specimens buckled before ultimate failure. The buckling mode was the same for each specimen, with a single half wave along the length of the specimen, with the maximum deflection at the center. The pre- and post-buckled deformations of the stringer rod and web of stringer specimen S04-1 are shown in Fig. 25a and 25b, respectively. The stiffener buckling mode across the specimens varied only in terms of the right-or-left orientation of the central buckle. The stringer specimen skins did not buckle prior to the buckling of the stiffener. After the stiffener buckled, the skin on the side toward which the stiffener buckled displaced toward the OML, while the skin on the opposite side displaced toward the IML. The pre- and post-buckled deformations of the skin of stringer specimen S04-1 are shown in Fig. 25c and 25d, respectively.

A similar series of PRSEUS single-stringer compression tests are reported in Ref. 10. The stringers described in Ref. 10 contained the same rod and overwrap as stiffener S07 herein, but did not display buckling behavior, and their shortening behavior was linear to failure in the range of -40 kips to -45 kips applied load. However, in this previous work, the stringer height was only 1.5 inches, compared to the 1.875-inch tall stringers in the current study. In addition, in the previous work, the stacks in the skin had the same orientation as the stacks in the stringer, causing the previous specimens to be stiffer than those reported here. The difference in the stiffnesses of the skin and stringer herein likely contributed to the specimens buckling due to a greater portion of the overall load being carried by the stiffener.

Because the same general buckling behavior occurred for each stringer specimen, each of the stringer specimens failed at the same location: the center of the specimen length. The extent of post-test damage for specimen S08-2 is shown in Fig. 26. The visible post-test damage in the skin tended to be highly localized to a single plane normal to the loading direction. Typically, for co-cured or co-bonded skin and stringers, the entire length of the stringer delaminates/disbonds.[11] The stitching present in the tested specimens kept the failure zone localized.

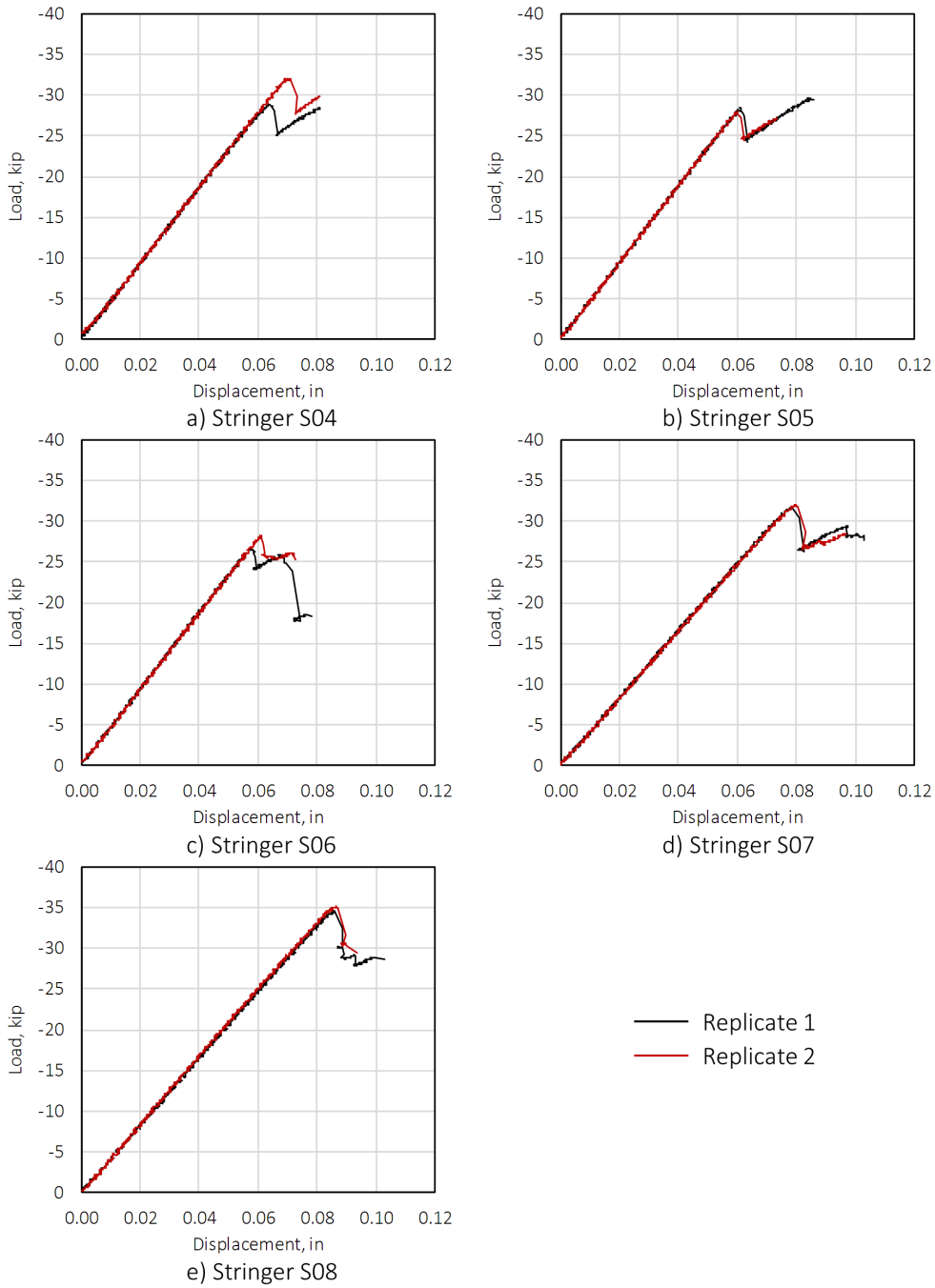

Figure 24. Stringer compression specimen load-displacement responses for all ten specimens.

The high-speed digital camera results revealed that the failures in the stringer specimens originated either at the fillets at the base of the stringer web or along the edges of the stringer flange. An example of failure propagation originating at the base of the stringer web is shown in Fig. 27 for specimen S04-1. The stiffener in specimen S04-1 buckled toward the second DIC system, causing the stringer rod to be out of the camera frame at the bottom of the images in Fig. 27. Damage propagated from the base of the stringer web up toward the rod before also propagating through the skin. The damage in the stringer web propagated up and around the rod in most cases, though the rod itself was not observed to break.

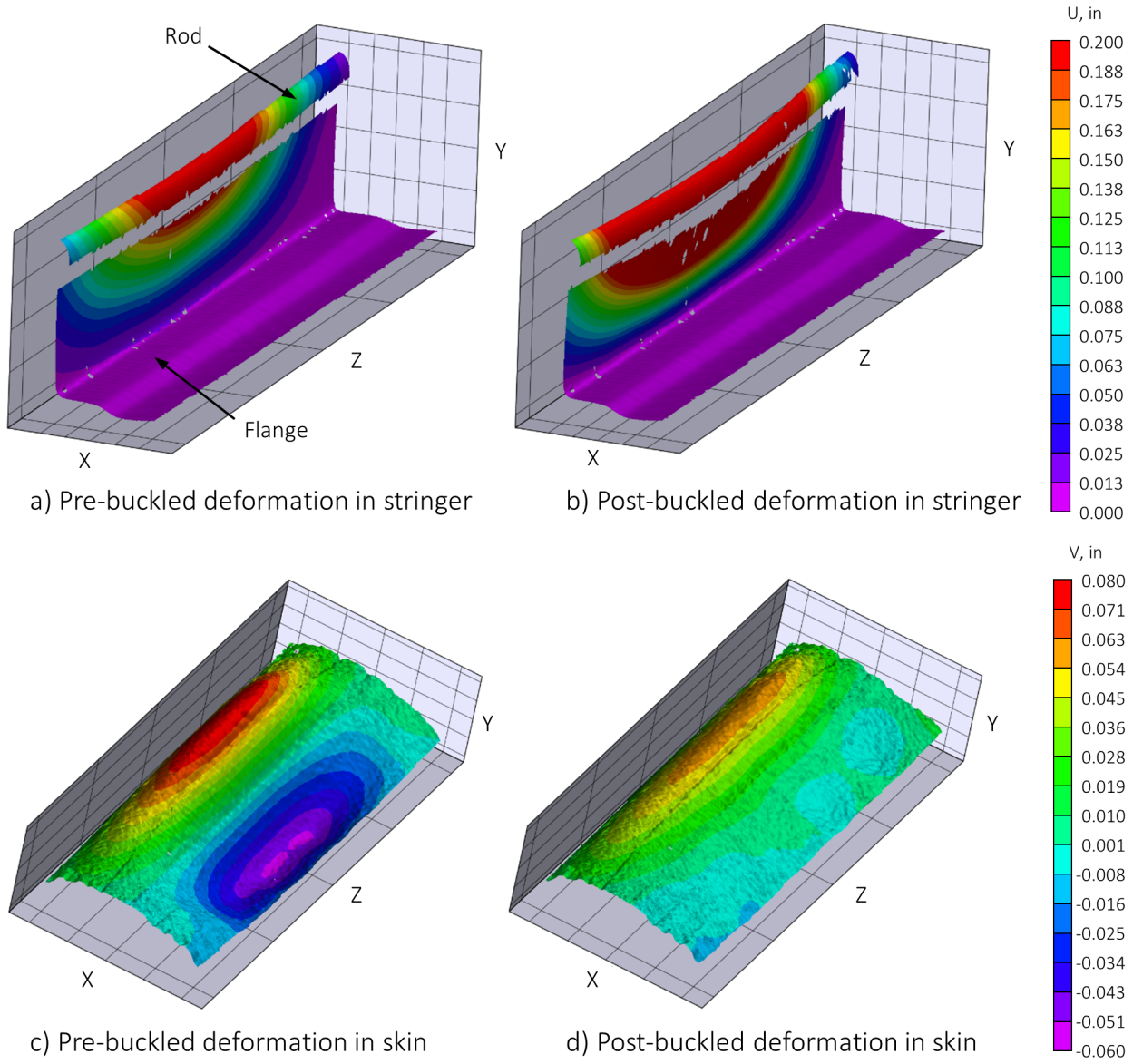

Figure 25. Pre- and post-buckled shapes of the single-stringer compression specimen S04-1.

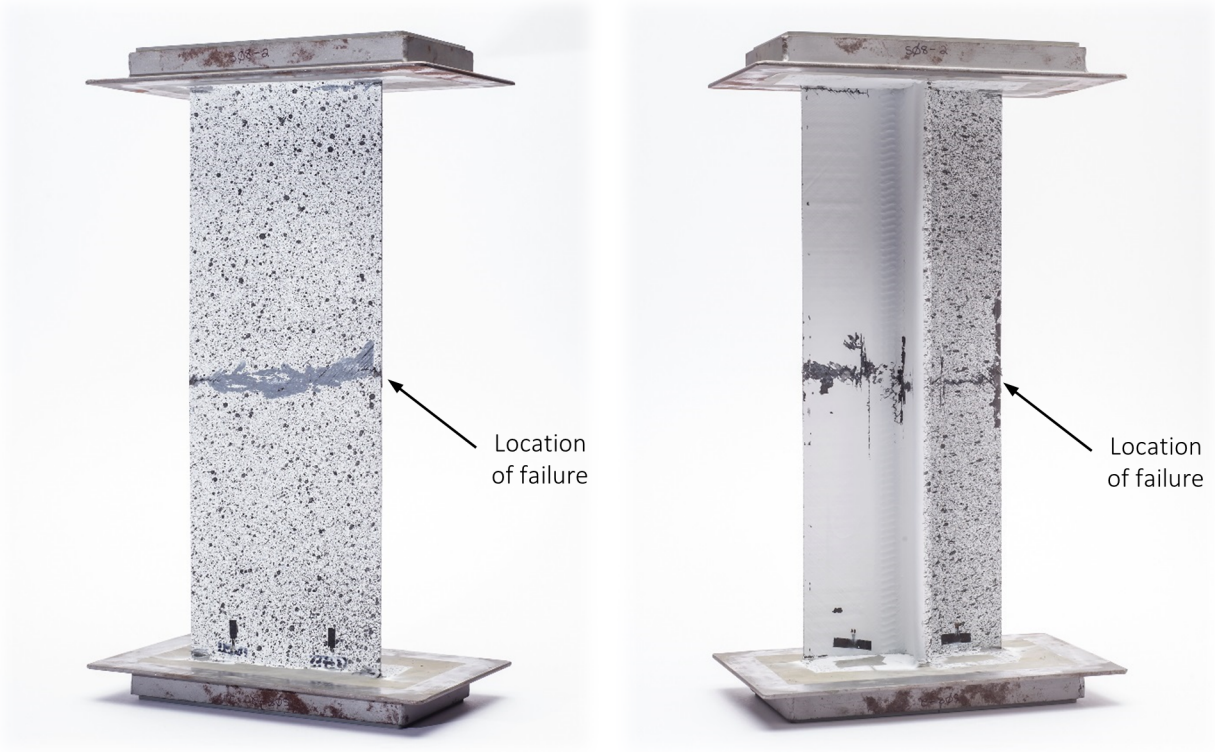

Figure 26. Post-test damage state for specimen S08-2.

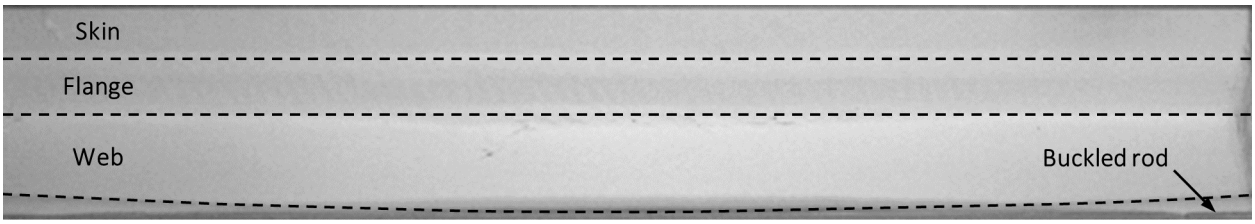

a) Δt = 0 μs

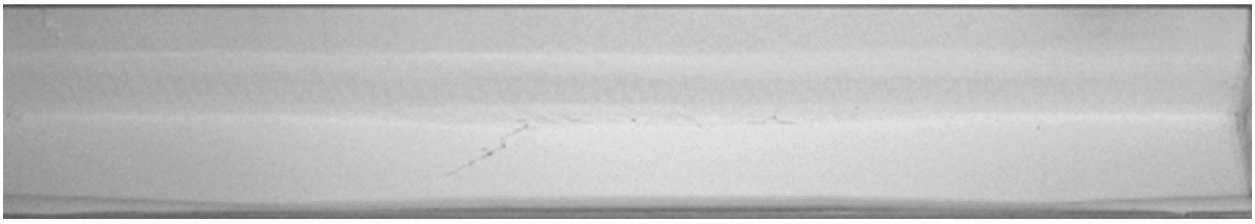

b) Δt = 66 μs

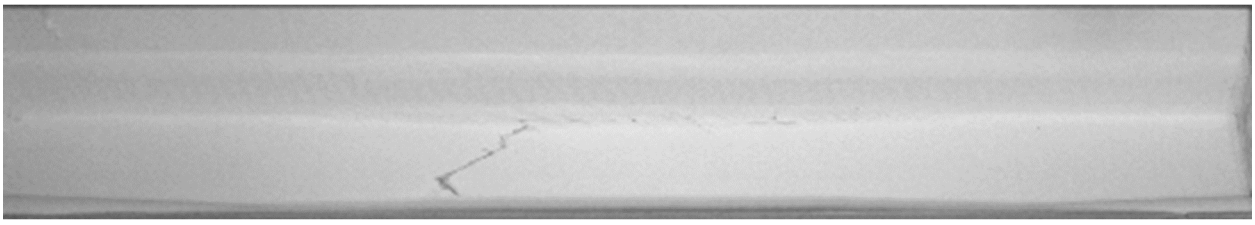

c) Δt = 100 μs

d) Δt = 250 μs

e) Δt = 333 μs

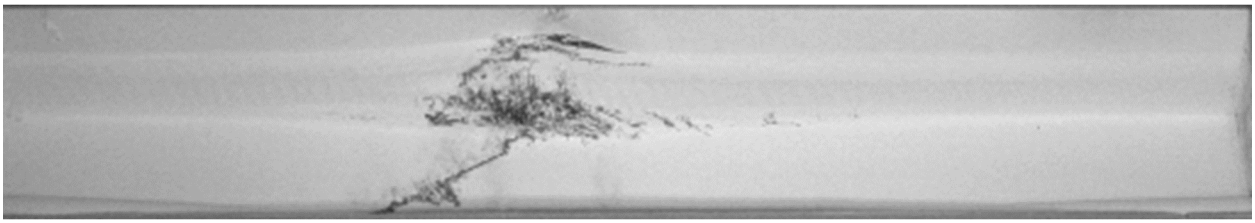

f) Δt = 716 μs

Figure 27. High-speed photography images of the failure of specimen S04-1.

D. Stringer Specimen Model

A finite element model of the single-stringer specimens was developed in order to further understand the failure process observed in the experiments. Because buckling was observed to be the triggering event of the stringer specimen failures, and all of the stringer configurations exhibited buckling, only the Class 72 configuration without adhesive was considered as a representative case.

The single-stringer analysis was solved in a single implicit dynamic step with Abaqus/Standard 6.13-1. Similar to the frame models, SC8R continuum shell elements were used to model the skin, tear straps, stringer flange, web, and overwrap. The rod was modeled using C3D8R solid elements. The model was 15.5-inches long, meant to represent the material between the potted ends of the specimens, and 5.7-inches wide. The stringer specimen anti-buckling guides were represented by constraining the y-direction displacement on the OML surface along two lines, 0.5 inch in from each free edge. The potted specimen ends were modeled by fully constraining the x-, y-, and z-direction displacements on one end, and the x- and y-direction displacements on the other. Compressive loads were introduced by monotonically displacing the nodes on one potted end of the model in the z-direction.

The predicted load-displacement response of the S07 stringer configuration model is shown in Fig. 28. Like the frame analyses, the stiffness of the single-stringer compression analysis overpredicted the experimental stiffness, likely due to overly stiff boundary conditions. Buckling was predicted to occur at approximately -37 kips applied load. This prediction is in good agreement with the average buckling load of -33.4 kips from the S07 and S08 stringer specimen tests reported in Table 2. After buckling, the model predicted the lateral displacement of the rod and overwrap to be approximately 0.12 inch at the center of the specimen, as shown in Fig. 29. The buckling of the stringer caused significant bending rotations at the two fillets located at the base of the stringer web. The bending at the base of the stringer web caused the $90°$-direction stresses to exceed the compressive allowable shortly after buckling, as shown in Fig. 30. At the next solution increment, the $90°$-direction stresses on the other side of the stringer web were predicted to exceed the tensile allowable. This prediction of damage initiating at the base of the stringer web agrees with the failure processes observed experimentally via high-speed video, e.g., Fig. 27.

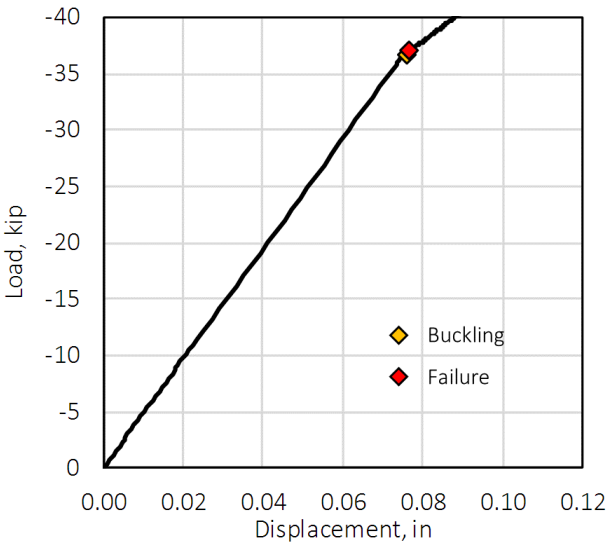

Figure 28. Load-displacement response from the analysis of the S07 stringer configuration.

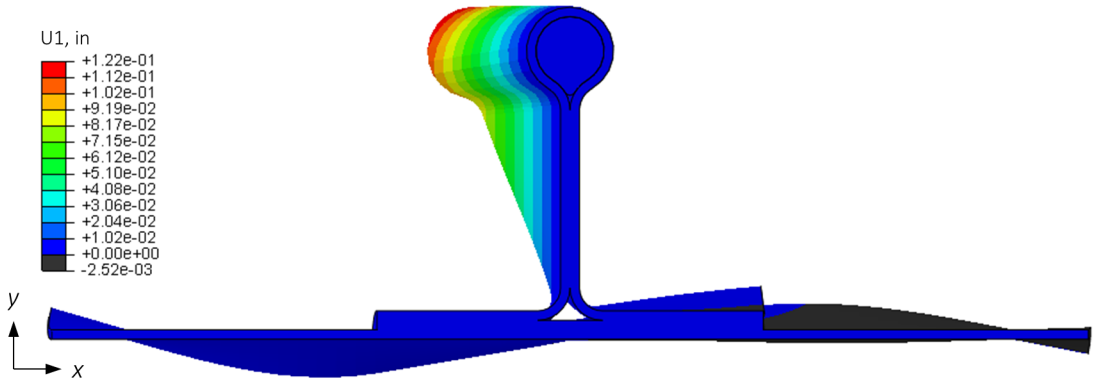

Figure 29. Contour plot from the analysis of the S07 stringer configuration, showing the lateral displacement of the rod immediately after buckling. The deformed shape is magnified five times for clarity.

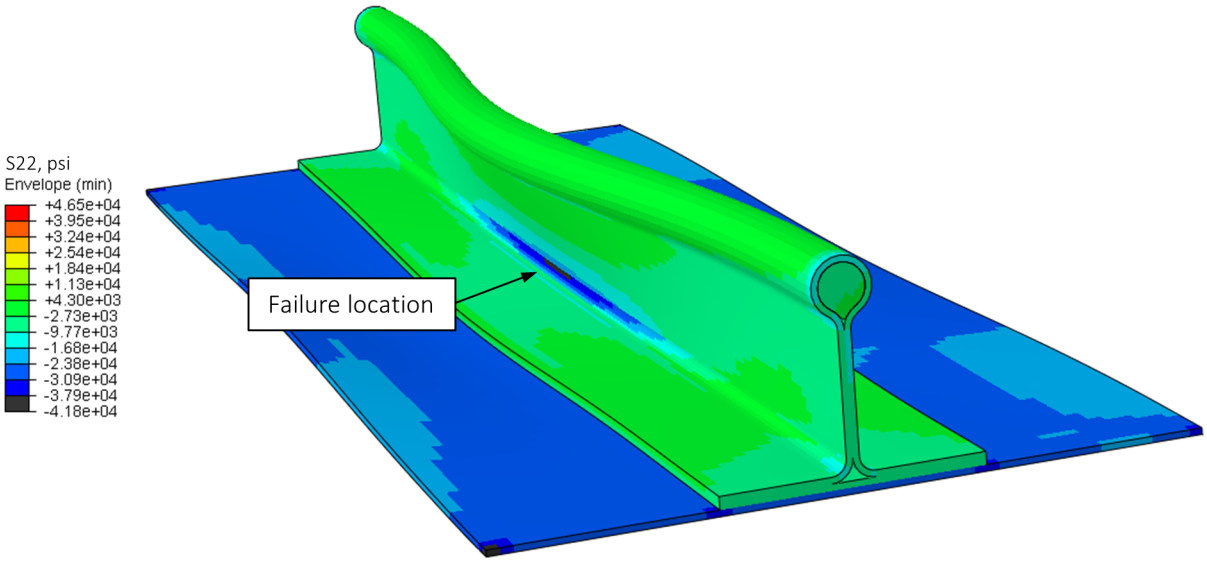

Figure 30. Contour plots from the analysis of the S07 stringer configuration, showing the 90°-direction stress upon exceeding the allowable. The deformed shape is magnified five times for clarity.

IV. Concluding Remarks

A series of tests were conducted on specimens harvested from a large stiffened panel containing a number of alternative design ideas for the application of the PRSEUS concept to frames, stringers, and T-caps. In this paper, the details of a set of single-frame compression and single-stringer compression tests and analyses were presented. All of the tested specimens performed well within the behavior predicted from pre-test expectations and analyses, based on specimen weight (i.e., heavier frames failed at higher loads than lighter frames) and intended application (i.e., hybrid wing body versus conventional fuselage). None of the tested specimens exhibited any unforeseen failure processes.

Of the tested frame configurations, the constant-thickness blade frame performed comparably to the foam-filled frame configuration which was used in the MBB test article. This finding indicates that it may be possible to utilize the PRSEUS concept for hybrid wing body applications without involving foam in the frame. The analysis of the constant-thickness blade frame supports this possibility, in that a linear load-displacement response was predicted well beyond the strength-based failure prediction, indicating that frame web buckling was not imminent, even without the sandwich configuration. The thinner, lighter, tapered-blade frame web post-buckled early in its load history, but continued to carry load without any load drops or severe nonlinearities until shortly before its ultimate failure.

The different stringer material configurations did not yield any significant differences in behavior. The tested specimens all exhibited buckling of the stringer to one side of the specimen, leading to failure at the center of the specimen at the point of maximum deflection. High-speed camera data revealed that the stringer failure process originated at the base of the stringer web. The stringer specimen analysis predicted the same buckling behavior, and indicated that the stringer buckling produced high stresses at the base of the stringer.

Acknowledgments

The authors would like to acknowledge the contributions of Ms. Teresa O'Neil for setting-up and performing the single-frame compression tests; Mr. George Cowley for setting-up and performing the single-stringer compression tests; and Dr. Nathaniel Gardner and Mr. Michael McNeill for setting-up and performing the optical measurements, and collecting and analyzing the data.

References

[1]Jegley, D. and Velicki, A., "Status of Advanced Stitched Unitized Composite Aircraft Structure," *51st AIAA Aerospace Sciences Meeting including the New Horizons Forum and Aerospace Exposition*, Grapevine, TX, Jan. 2013.

[2]Velicki, A., "Damage Arresting Composites for Shaped Vehicles, Phase I Final Report," NASA/CR-2009-215932, NASA Langley Research Center, Hampton, VA, Sept. 2009.

[3]Velicki, A., Yovanof, N., Baraja, J., Linton, K., Li, V., Hawley, A., Thrash, P., DeCoux, S., and Pickell, R., "Damage

Arresting Composites for Shaped Vehicles—Phase II Final Report," NASA/CR-2011-216880, NASA Langley Research Center, Hampton, VA, Jan. 2011.

[4]Linton, K., Velicki, A., Hoffman, K., Thrash, P., Pickell, R., and Turley, R., "PRSEUS Panel Fabrication Final Report," NASA/CR-2014-218149, NASA Langley Research Center, Hampton, VA, Jan. 2014.

[5]Jegley, D., Rouse, M., Przekop, A., and Lovejoy, A., "The Behavior of a Stitched Composite Large-Scale Multi-Bay Pressure Box," NASA/TM-2015-218972, NASA Langley Research Center, Hampton, VA, Nov. 2015.

[6]Lovejoy, A. and Leone, F., "T-cap Pull-off and Bending Behavior for Stitched Structure," NASA/TM-2015-218971, NASA Langley Research Center, Hampton, VA, Nov. 2015.

[7]Leone, F., "Pultruded Rod/Overwrap Testing for Various PRSEUS Stringer Configurations," NASA/TM-2015-218975, NASA Langley Research Center, Hampton, VA, Nov. 2015.

[8]Velicki, A., Hoffman, K., Linton, K., Thrash, P., Pickell, R., and Turley, R., "Fabrication of Lower Section and Upper Forward Bulkhead Panels of the Multi-Bay Box and Panel Preparation," NASA/CR-2015-218981, NASA Langley Research Center, Hampton, VA, Nov. 2015.

[9]ABAQUS, *Abaqus 6.13 Online Documentation*, Dassault Systèmes, Providence, RI, 2013.

[10]Jegley, D., "Experimental Behavior of Fatigued Single Stiffener PRSEUS Specimens," NASA/TM-2009-215955, NASA Langley Research Center, Hampton, VA, Dec. 2009.

[11]Jegley, D., Velicki, A., and Hansen, D., "Structural Efficiency of Stitched Rod-Stiffened Composite Panels with Stiffener Crippling," *49th AIAA/ASME/ASCE/AHS/ASC Structures, Structural Dynamics and Materials Conference*, Schaumburg, IL, April 2008.